Forschungszentrum Karlsruhe
Technik und Umwelt

Wissenschaftliche Berichte
FZKA 5927

MHD Flow and Heat Transfer in a Rectangular Duct

L. Barleon, U. Burr, M. Frank, R. Stieglitz, K.-J. Mack
Institut für Angewandte Thermo- und Fluiddynamik
Projekt Kernfusion

Februar 1998

Forschungszentrum Karlsruhe

Technik und Umwelt

Wissenschaftliche Berichte

FZKA 5927

MHD Flow and Heat Transfer in a Rectangular Duct

L. Barleon, U. Burr, M. Frank, R. Stieglitz, K.-J. Mack

Institut für Angewandte Thermo- und Fluiddynamik
Projekt Kernfusion

Forschungszentrum Karlsruhe GmbH, Karlsruhe
1998

Als Manuskript gedruckt
Für diesen Bericht behalten wir uns alle Rechte vor

Forschungszentrum Karlsruhe GmbH
Postfach 3640, 76021 Karlsruhe

Mitglied der Hermann von Helmholtz-Gemeinschaft
Deutscher Forschungszentren (HGF)

ISSN 0947-8620

Abstract:

Only the knowledge of the convective-diffusive heat transport phenomena in laminar and turbulent MHD flows enables an adequate design of heat transfer units (e.g. liquid metal cooled fusion blankets) or the development of MHD controlled processes. This report presents an experimental and numerical study of the heat transfer in a flow of a rectangular duct with electrically conducting walls exposed to an uniform transverse magnetic field B, oriented parallel to two walls. The heat flux $\dot{q}$ produced by a radiation heater is perpendicular to B. Both, the integral quantities (pressure drop, Nusselt number Nu) as well as the local ones (temperature at fluid-wall interface, velocity, temperature in the fluid) are measured. The parameters investigated are: Hartmann number $0 \leq M \leq 5000$, Reynolds number $0 \leq Re \leq 1.3 \cdot 10^5$ and Peclèt number $0 \leq Pe \leq 2900$.

The measured pressure drop agrees with the analytic one for two-dimensional laminar duct flows for nearly all parameters. Only for $M \leq 350$ and $Re \geq 7 \cdot 10^4$ higher values are obtained. The critical Reynolds number Re_{crit} where the pressure drop of the MHD flow is negligibly small compared with an ordinary hydrodynamic flow (OHD) is found to be given in the investigated configuration by the relation $Re_{crit} = 100 \cdot M$. Regarding the velocity distribution and the temperature distribution within the duct, which are measured using a temperature-potential probe (TEMPO), an excellent agreement between experiment and calculation is found for laminar MHD flows. The wall Nusselt number of the MHD flow is due to the high velocity jet at the walls parallel to B about 30% higher compared to an ordinary hydrodynamic flow. At high M and for large Re and Pe the same heat transfer characteristics as in a laminar MHD flow is found because the thermal boundary layer has not left the viscous laminar sublayer of the jet and thus the heat transfer is still based on pure heat conduction in this sublayer. If the duct is long enough or the parameter constellation is chosen properly so that the thermal boundary layer exceeds the viscous sublayer of the jet the heat removal is enhanced by a factor of 2 compared to a laminar MHD flow.

MHD Strömung und Wärmeübergang in einem Rechteckkanal

Zusammenfassung:
Lediglich eine profunde Kenntnis des Wärmeübertragungsverhaltens laminarer und turbulenter magnetohydrodynamischer (MHD) Strömungen erlaubt eine adäquate Auslegung von Wärmeübertragern, zum Beispiel von Flüssigmetallblankets, oder eine Steuerung industrieller Verfahren durch den Einsatz von MHD Effekten.
In diesem Bericht wird die experimentelle und numerische Untersuchung einer MHD-Strömung in einem Rechteckkanal mit elektrisch leitenden Wänden vorgestellt. Ein äußeres konstantes Magnetfeld B steht senkrecht auf der Kanalachse und ist ebenfalls senkrecht zum Wärmestrom $\dot{q}$, der von einem Strahlungsheizer erzeugt wird. Im Kanal werden sowohl integrale Größen wie der Druckverlust und die Nusselt-Zahl aber auch lokale Größen, zum Beispiel die Temperatur an der Fluid-Wand-Grenzfläche, die Geschwindigkeit und die lokale Temperatur ermittelt. Der untersuchte Parameterbereich umfaßt: Hartmann-Zahlen $0 \leq M \leq 5000$, Reynolds-Zahlen $0 \leq Re \leq 1.3 \cdot 10^5$ und Peclèt- Zahlen $0 \leq Pe \leq 2900$.
Der gemessene Druckverlust stimmt mit der analytischen Lösung für eine zweidimensionale MHD in nahezu dem gesamten untersuchten Parameterbereich überein. Lediglich für Hartmann-Zahlen $M \leq 350$ und $Re \geq 7 \cdot 10^4$ wird ein höherer Druckverlust ermittelt. Beim Überschreiten einer kritischen Reynoldszahl Re_{crit} von $Re_{crit} \approx 100 \cdot M$ entspricht der MHD-Druckverlust dem einer turbulenten hydrodynamischen Rohrströmung. Die Temperatur- und Geschwindigkeitsverteilung im Kanal, die mit einer kombinierten Temperatur- und Geschwindigkeitsmeßsonde (TEMPO) ermittelt wurde, stimmt mit den berechneten Werten für eine laminare MHD-Strömung überein. Die Nusselt-Zahl an der Wand ist bei MHD-Strömungen aufgrund der wandnahen Geschwindigkeitsüberhöhungen (, den sogenannten Seitenwandjets), die sich an Wänden parallel zum Magnetfeld ausbilden und direkt dem Wärmestrom ausgesetzt ist, um ca. 30% größer als in einer hydrodynamischen Strömung. Bei großen M und sehr großen Re entspricht der Wärmeübergang der turbulenten MHD Strömung dem Wärmeübergang wie er auch in einer laminaren Strömung ermittelt wird. Der Grund dafür ist, daß die thermische Grenzschicht sich noch im Bereich der viskosen laminaren Grenzschicht befindet und somit leistet lediglich die molekulare Wärmeleitung einen Beitrag zur Wärmeübertragung. Bei bestimmten Parameterkonstellationen oder bei hinreichend langen Kanälen wächst die Grenzschicht in den Bereich der turbulenten Seitenwandschichten hinein. Durch den turbulenten Quertransport des Fluids wird der Wärmeübergang gesteigert. Die Wärmeübertragungsverbesserung kann um den Faktor 2 höher sein als bei einer laminaren MHD-Strömung.

Contents

Chapter 1

Introduction

Liquid metals are often considered as coolant for an efficient heat removal of thermally high loaded surfaces because of their high thermal molecular conductivity. Therefore, they facilitate rather simple geometries of heat transfer units. In the fusion technology the use of Lithium or Lithium alloys as coolants of the plasma facing structure, called the blanket, offers additionally the breeding of Tritium the 'fuel' for fusion. But, if an electrically conducting fluid flows in the strong, fusion plasma confining, magnetic field $\vec{B}$ it experiences a body force opposing the fluid motion. This body force known as Lorentz force arises from the electric currents $\vec{j}$ induced by the fluid motion, according to the cross product $\vec{v} \times \vec{B}$, and interact themselves with the magnetic field $\vec{B}$. The magnitude of the Lorentz force is determined by the electric conductivity both, of the fluid and the wall. The interaction of these vector fields velocity, magnetic field and electric current density forms magnetohydrodynamics (MHD), which yields velocity distributions, turbulence structures and pressure fields unknown in ordinary hydrodynamics (OHD). Consequently, any optimization of industrial fabrications processes by means of MHD has to focus on the named vector fields, which involves in addition to OHD not only the molecular thermo-mechanical properties of the system fluid/wall, but also the electric properties.
Similarity considerations for the heat transfer of a magnetohydrodynamic duct flow result in the following five dimensionless parameters, the magnetic Reynolds number R_m, the Hartmann number M, the interaction parameter N, the Peclèt number Pe, and the wall conductance ratio c:

$$R_m = \mu\sigma v_0 a; M = aB_0\sqrt{\frac{\sigma}{(\rho\nu)}}; N = \frac{a\sigma B_0^2}{\rho v_0}; Pe = \frac{v_0 a}{\kappa}; c = \frac{\sigma_w t_w}{\sigma a}. \qquad (1.1)$$

Here, μ, σ, ρ, ν, κ are the magnetic permeability, the electric conductivity, the density, the kinematic viscosity and the molecular heat diffusivity of the fluid; a is a characteristic length of the duct cross-section; σ_w and t_w are the electric conductivity and the thickness of the duct walls; B_0 is the magnetic field strength and v_0 the average velocity in the duct.

The magnetic Reynolds number R_m expresses the ratio of the magnetic field induced by the currents to the externally applied magnetic field and is assumed to be negligibly small. The field B_0 can be assumed to be constant. The Hartmann number M and the interaction parameter N weight the electromagnetic force to the viscous and the inertial forces, respectively. For fusion typical applications usually M and N are of the order $10^2 - 10^5$, see Holroyd&Mitchell (1984). The classical Reynolds number Re can be obtained by the relation M^2/N. An energy balance leads to the Peclèt number which describes the ratio of the convective to the diffusive heat transport. Liquid metals are characterized by small Prandtl numbers Pr ($Pr = \nu/\kappa$) of the order $10^{-3} - 10^{-2}$ so that the Peclèt number varies in the field of fusion technology typically from $10^1 - 10^3$. Since the magnitude of the induced electric currents significantly influences the pressure drop in a duct the wall conductance ratio c, which describes the electric conductivity of the wall compared to that of the fluid, is as small as possible with values of $O(10^{-2} - 10^{-1})$.

Before outlining some results for MHD flows in rectangular ducts which have been obtained in the past by numerous authors, some characteristic phenomenological aspects are discussed.

Consider the flow in a rectangular duct as shown in figure 1-1a. The duct consists of two walls aligned with the magnetic field and two walls being perpendicular to the magnetic field. The fluid flows in positive x-direction inducing an electric field, which is proportional to $\vec{v} \times \vec{B}$. The resulting potential difference drives an electric current $\vec{j}$, which interacts with the magnetic field producing the Lorentz force ($\vec{j} \times \vec{B}$) opposing the fluid motion.

Order of magnitude estimates by Holroyd&Walker (1978) and Grinberg (1985) show that at high Hartmann numbers and interaction parameters the MHD flow in a rectangular electrically conducting duct develops quite fast, namely in a length l_{dev} of the order $O(\sim 1/\sqrt{c})$ after entering the homogeneous magnetic field region. However, this hypothesis is up to now not experimentally proved.

A characteristic feature of two-dimensional MHD flows in rectangular ducts at $M \gg 1$ is that most of the ducts cross-section is occupied by a *core* flow, which is of slug flow type. In this *core* a balance of pressure forces and Lorentz-forces exists. Between the *core* and the walls boundary layers appear both different in form and extension. At walls perpendicular to $\vec{B}$, named Hartmann walls, the Hartmann layers appear. These layers are rather thin with a thickness of δ_H of $O(1/M)$. There, the pressure forces and the Lorentz forces are acting against the viscosity of the fluid. At walls parallel to the magnetic field, called *side walls*, the *side layers* are present. Within these layers Lorentz-forces play to the first order no role. The thickness of the side layers δ_S scales with $\delta_S \sim 1/\sqrt{M}$. Different to the Hartmann layers, which are characterized by an exponential decay of the velocity towards the wall, in the side layers high velocity jets are possible, which depend only on the ratio of the Hartmann wall conductance to the side wall conductance, i.e. c_H and c_S. Even a flow reversal within these side layers is possible as reported by Hunt (1965). The flow rate carried by the side layers is $O(1)$ and can be higher than that of the core flow. Two analytically calculated velocity profiles for the duct geometry studied in the experiment are shown in figure 1-1b, c.

The layer structure of fully developed MHD flows has been shown in principle by Hunt et al. (1969) and Branover et al. (1978a). Since the scaling of these layers depends strongly on the Hartmann number M their measurements have been restricted to relatively small Hartmann numbers $M \lesssim 50$.

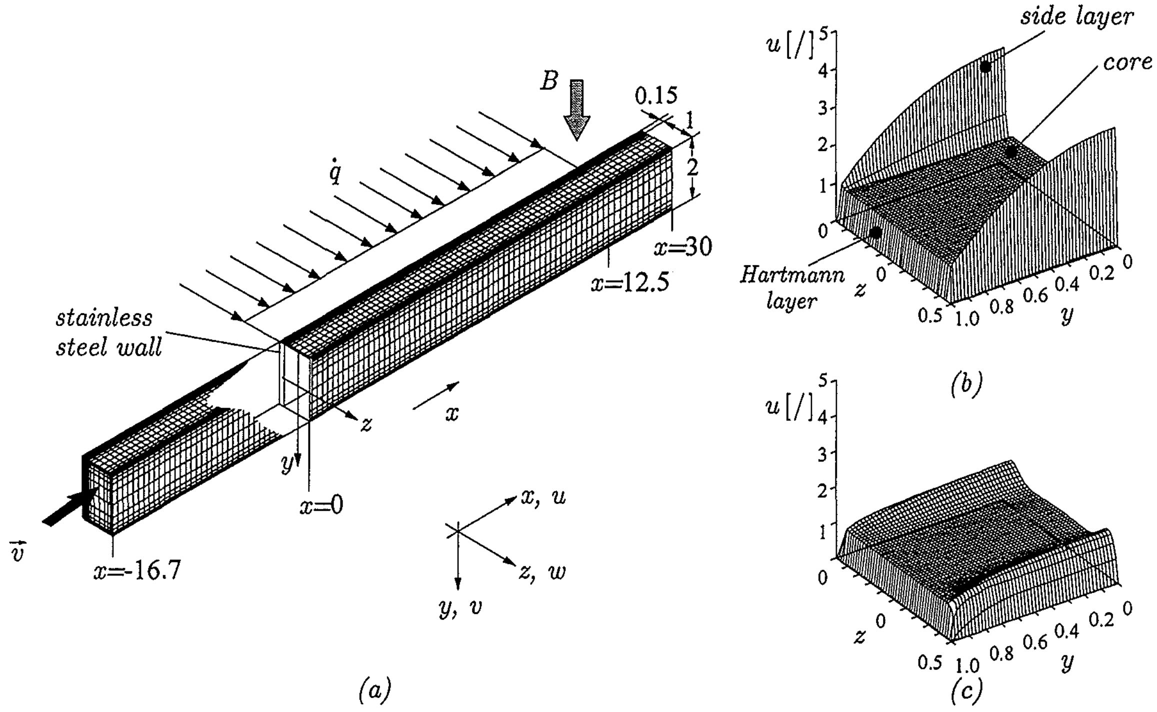

Figure 1-1 (a) Schematics and coordinate system of the duct studied. The mesh imbedded in the figure shows the computational mesh being used in the numerics. The profiles of the mean streamwise velocity in the figures (b) and (c) are calculated for $c_s = 0.0714$ and $c_H = 0.0119$ and for the Hartmann numbers $M = 4940$ (b), $M = 350$ (c).

Although a large scientific community is investigating isothermal MHD flows in quite complex geometries it is noteworthy that only a few works, mostly theoretical ones, about MHD heat transfer mechanisms are published. An analytic solution for the heat transfer in a laminar 2D MHD pipe flow has been given by Gardner (1967) for a very specific set of boundary conditions. An overview over the heat transfer in laminar 2D-MHD duct flows for different duct geometries, electric wall conditions and thermal boundary conditions is given in the book of Blums et al. (1987). This book focuses mainly on the analytical formulation of solutions of the heat transfer in MHD boundary layers, which is the most important problem due to the complexity of these layers compared to the slug flow profile present in the core. Unfortunately most MHD heat transfer duct flow problems in rectangular geometries with electrically conducting walls can not be solved analytically so that numerical methods have to be applied, see e.g. Bühler (1993).

In most technical applications however, the flow is thermally developing before reaching the outlet of the heated section. Similarity considerations yield that the thickness of the thermal boundary layer δ_{th} scales with $\delta_{th} \sim 1/\sqrt{Pe}$. Consider now a duct flow with a Peclèt number $Pe = 10^4$ and duct dimensions of approximately 0.1m in the geometry shown in figure 1-1. If we scale the Peclèt number with the heated length, namely the $x-$coordinate, the flow is thermally developed if the thermal boundary layer has reached the opposite side. This results in a thermal development length of $O(10m)$! This simple estimate demonstrates the necessity for the detailed study of thermally developing flows.

In figure 1-2 a sketch of the growth of the developing thermal boundary layer with the viscous MHD side wall layer is shown. The high velocity jet in the side layer which carries an $O(1)$ flow rate allows an excellent heat removal from the wall compared to a hydrodynamic flow. So the Nusselt numbers attainable in laminar MHD flows are higher than in laminar OHD flows.

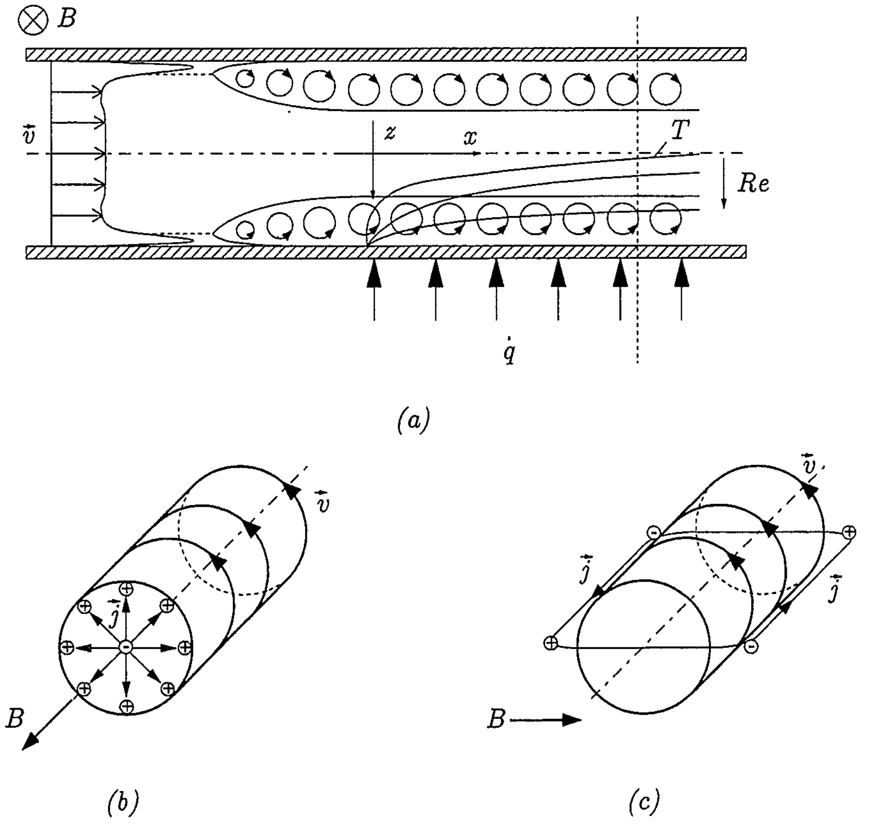

Figure 1-2 a) Sketch of the development of the thermal boundary layer in the duct in dependence of the Reynolds number. b.) This subgraph shows the mechanisms of the destruction or conservation of vortices under the influence of the magnetic field.

In order to explain the heat transfer mechanisms properly it is necessary to understand the dynamics of the MHD flow in detail especially if it gets turbulent, because here also MHD reveals features not present in OHD.

Despite the fact that magnetic fields have a stabilizing effect on the flow of conducting fluids, the flow in most ducts are turbulent, especially in heat transfer units. An approach to describe the turbulent fluid motion in MHD flow in rectangular ducts is elaborated by Cuevas et al. (1996, 1997). There, the flow regimes are investigated using a composite core-side layer spectral collocation method which resolves except for the Hartmann layers each flow domain. The turbulent velocity profiles are obtained using an iterative scheme in which the turbulence is introduced through an eddy viscosity model. The results obtained reveal features also found in the present experiment.

Nevertheless, also disagreements appear and a closed MHD turbulence model is still lacking. The reasons are quite obvious. First, integral and locally reliable measurements of turbulent MHD flows even in simple geometries do not exist. Second, MHD flows are highly anisotropic, which arises from the anisotropic character of the electromagnetic forces. If only the local turbulence structure like the formation and decay mechanisms of vortices in MHD-flows would be known, a first step towards the development of a semi-empirical description of the isothermal turbulent MHD transport phenomena could be made. Right now, only the model of Cuevas et al. (1997), which is also extended to the turbulent heat transfer (1997b) shows satisfactory results.

Within this article the authors focus only on the description of the characteristic features of magnetohydrodynamic turbulence. Further information about the experimentally found specific phenomena of MHD-turbulence the experimental results are reported in the articles of Kolesnikov&Tsinober (1972), Lielausis (1975), Reed&Lykoudis (1978), Reed&Picologlou (1989). Still unsatisfactory theoretical attempts to describe the phenomena being observed in the experiments are given in Branover (1978a), Davidson (1995), Sommeria&Moreau (1982). The given references are of elective nature and by far not complete; an overview with cross references may be taken from Moreau (1990) and Tsinober (1989).

Consider a shear flow as appearing in the side layer jet of a MHD duct flow (see figure 1-1b or figure 1-22a). If the shear stress, expressed by τ, which is proportional to $\partial v/\partial z$ exceeds a certain value, vortices are generated. In MHD flows at high Hartmann numbers the structure of these vortices is in principle two-dimensional. (However, slight three-dimensional time dependent flow patterns may appear in the regions where the core-flow matches the wall adjacent boundary layers. However, an experimental evidence is not available yet.) The axis of the large vortex is aligned with the magnetic field lines. The reason why MHD flows tend to form such a 2D structure can be easily explained by the figures 1-2b and 1-2c.

Let us consider first a vortex as shown in figure 1-2b with the rotation axis being parallel to B. Due to the interaction of v and B within the vortex an electric potential is induced, in which iso-velocity lines are iso-potentiallines. Since the induced currents are azimuthal, the current paths automatically close on themselves. The azimuthal torque destroying the vortex disappears if the gradient of the angular momentum in direction of B is zero. Physically, this arises because the possible electric current points radially outwards and is independent of z. By symmetry, this current has no means of recirculating and so the cross-product of the azimuthal velocity and B is exactly balanced by a radial gradient in the electric potential. However, near the top and bottom of the vortex the current can return through regions of small or zero swirl.

The resulting in- and outward flow at the boundaries gives rise to a reversed azimuthal torque which in turn creates a positive angular momentum in previously stagnant zones. So there is an exchange of swirl and motion perpendicular to B stretching the vortex in direction of magnetic field lines. This is finally limited in a duct flow by the Hartmann walls, in which the current loops can close and viscous dissipation becomes important. An energy analysis shows that the Joulean losses of the vortex are minimized if the velocity perpendicular to the magnetic field in the vortex disappears, so that the vortex behaves like a rotating rigid body.

Consider next a vortex with an axis normal to B. The velocity field induces due to the orientation of B an electric current j, which interacts itself with B leading to a Lorentz-force distorting and finally destroying the vortex.

A detailed analysis of the temporal and spatial development of vortices and how they are damped by means of the magnetic field is extensively described by Davidson (1995). Here, the authors repeat and analyze shortly the main statements of this article.

- The Lorentz force destroys kinetic energy but does not alter the net linear and angular momentum of the fluid. Resulting from this the pressure drop in turbulent MHD duct flows differs not significantly from laminar one even for low interaction parameters as $M \gg 1$.
- The Lorentz-force tends to direct the flow in such a way that the relative dissipation continually falls. This however, is realized by elongating the flow along magnetic field lines.
- The spreading of momentum and vorticity along field lines is essentially a diffusive process.

By now it is unclear at which parameters primary vortices appear and the flow gets unstable. A dimensional analysis immediately shows that Hartmann number, interaction parameter and ,in case of electrically conducting walls, the wall conductance ratio of the Hartmann walls c_H are the leading parameters. In fact, measurements in a conducting rectangular duct performed by Reed&Picologlou (1989) demonstrated that the side wall jets get instable exceeding a critical Reynolds number. But, the time dependent flow domain in their measurements is confined to the side wall region whereas the core flow remains laminar. Moreover, in contradiction to the book of Branover (1978b) they found that the onset of instability is only *marginally* dependent on the Hartmann number if $M \gg 1$. A similar result is also found in our measurements, see §4.1, where a weak dependence of the critical Reynolds number on M is shown.

A linear stability analysis which is directly related to the experiment mentioned above has been performed by Ting et al. (1991). The result of the analysis is that the side wall jet is instable for a critical Reynolds number $Re_{crit} = 343$, which is one order of magnitude lower than found in the experiments. The critical Reynolds number predicted is independent of M. The disagreement between analysis and experiment is based on the different shape of the side layers, which is an input parameter in the analysis. There, the analytically calculated velocity profile for $M \gg 1$ is used as base solution for the perturbations, whereas in the experiment such a shape of the velocity profile has not been found.

In this report the laminar and turbulent MHD flow in a rectangular duct with thin conducting walls exposed to a uniform magnetic field B and an applied heat flux $\dot{q}$ perpendicular to the magnetic field B is investigated for the following parameters:

- $0 \leq M \leq 5 \cdot 10^3$;
- $0 \leq Re \leq 1.3 \cdot 10^5$;
- $0 \leq Pe \leq 2900$.

The aim of this paper is to investigate the hydraulic properties of the investigated test module in terms of

- pressure gradient dp/dx as a function of M and N;
- velocity distribution u in flow direction within the liquid as a function of M and N.

The heat transfer from the wall and within the liquid is investigated for the leading parameters. Therein, the specific features of turbulence in MHD are outlined. The report is organized in such a way that in section §2.1 the problem is formulated and in the paragraph §2.2 the solution methods and specific strategies are explained. After the description of the experimental setup in §3 the obtained results are discussed for the isothermal MHD flow in §4.1. Subsequently in §4.2, the heat transfer in the MHD flow is discussed. An attempt to extrapolate the heat transfer results to a blanket design is made in §4. Finally, the conclusions are drawn.

Chapter 2

Formulation and Analysis

2.1 Formulation

The investigated duct flow has a rectangular shape as shown in figure 1-1. The dimensionless equations governing the MHD flow in the inductionless limit as $R_m \rightarrow 0$ are the conservation of :

- momentum

$$\frac{1}{N}\left(\frac{\partial \overrightarrow{v}}{\partial t} + (\overrightarrow{v} \cdot \nabla)\,\overrightarrow{v}\right) = -\nabla p + \frac{1}{M^2}\Delta \overrightarrow{v} + \overrightarrow{j} \times \overrightarrow{B}, \tag{2.1}$$

- energy

$$Pe\left(\frac{\partial \Theta}{\partial t} + (\overrightarrow{v} \cdot \nabla)\,\Theta\right) = \Delta\Theta, \tag{2.2}$$

- mass

$$\nabla \cdot \overrightarrow{v} = 0, \tag{2.3}$$

- charge

$$\nabla \cdot \overrightarrow{j} = 0, \tag{2.4}$$

- and Ohm's law

$$\overrightarrow{j} = -\nabla\Phi + \overrightarrow{j} \times \overrightarrow{B}. \tag{2.5}$$

Here, v, t, p, j, B, Θ and Φ denote the dimensionless velocity, the time, the pressure, the electric current density, the magnetic induction, the temperature difference and the electric potential scaled with the values v_0, a/v_0, $a\sigma v_0 B_0^2$, $\sigma v_0 B_0$, B_0, $(\dot{q} \cdot a)/\lambda$

and av_0B_0, respectively. ΔT is a characteristic temperature difference. Here, ΔT is the difference between the average inlet temperature and the average temperature at the measurement position.

The magnetic field is assumed to be uniform and constant. Moreover, for simplicity a non-buoyant flow is considered so that the molecular properties of the liquid like the density ρ, the kinematic viscosity ν, the specific electric conductivity σ, the heat capacity c_p and the heat conductivity λ are constant with respect to space and time. As a result of this assumption the temperature Θ acts like a passive scalar. Finally, an order of magnitude estimate shows that the Ohmic heating is negligible in electrically well conducting liquids. This enables us to decouple the current density $\vec{j}$ from the energy equation.

The boundary conditions on the walls are the non-slip condition,

$$\overrightarrow{v}|_w = 0, \tag{2.6}$$

and the thin-wall condition, see e.g. Walker (1981)

$$\overrightarrow{j} \cdot \overrightarrow{n} = c\nabla_{\perp}^2 \Phi_w, \tag{2.7}$$

where $\vec{n}$ is the unity vector normal to the wall and $\nabla_{\perp}$ denotes the projection of the gradient on the wall surface. The thin-wall condition describes the balance of charge in the conducting duct walls. The currents $(\vec{j} \cdot \vec{n})$ leaving the fluid to the wall enter this balance as a source term. If the fluid is in perfect electrical contact with the duct walls, that means there is no contact resistance across the fluid-wall interface, the potential of the wall and that of the adjacent fluid are equal, i.e.

$$\Phi = \Phi_w, \tag{2.8}$$

at the interface. At the inlet and the outlet of the test section a fully developed two-dimensional MHD-flow is assumed.

Regarding heat transfer, the same conditions as in hydrodynamics are applied. For a given constant heat flux of $\dot{q}$ perpendicular to the magnetic field the temperature condition reads

$$\frac{\partial \Theta}{\partial n} = \dot{q} \, . \tag{2.9}$$

If the heat conducting wall is of finite thickness the highest temperatures appear at the outside of this wall. This temperature $\Theta_{w,o}$ can be calculated with the relation

$$\Theta_{w,o} = \Theta_{w,i} + \frac{1}{Bi}\, \dot{q}, \tag{2.10}$$

where $\Theta_{w,i}$ is the dimensionless temperature at the fluid-wall interface and Bi is the Biot number, which is defined by

$$Bi = \frac{\lambda_w a}{\lambda t_w}. \tag{2.11}$$

Finally, the flow is assumed to be fully developed both at the inlet and at the outlet. Consequently, the electric current in flow direction is zero. The derivatives of the velocity vanish $x-$direction and also the pressure gradient keeps constant.

2.2 Analysis

As mentioned in the formulation the temperature is a passive scalar if buoyant effects are neglected. Assuming a fully developed two-dimensional (2D) flow at the inlet and the outlet the velocity/pressure-field and the temperature field can be separately investigated. The following strategy is used to calculate the laminar heat transfer in a rectangular duct:

- The velocity field is calculated using an analytical solution valid for 2D MHD flows.
- A non-equidistant mesh in all coordinate directions is generated with a commercially available program package.
- The values for the velocity are interpolated on that mesh.
- The heat transport in both wall and fluid is calculated on the mesh for the given boundary conditions using the commercial program package *FIDAP*.

In the following two subsections the main features of the MHD program and the numerics being used are shortly described. Further information may be taken from the literature cited.
For the OHD duct flow, which is also presented, a different procedure is used. The solution is obtained completely numerically using the *FIDAP* program package. The results calculated are displayed in the second subsection of this chapter.

2.2.1 Analytical 2D-MHD duct flow

The velocity and pressure field of the two-dimensional fully developed MHD flow in the studied geometry is treated by means of an analytic solution presented by Molokov (1993). Here the main features of this solution are outlined:

- The applied magnetic field B is supposed to be strong, i.e. $M \gg 1$;
- the magnitude of the wall conductance ratio of the side wall c_S is arbitrary, including the limiting cases of insulating and perfectly conducting walls;
- the Hartmann walls are much better electrically conducting than the adjacent Hartmann layers, i.e. $c_H \gg 1/M$, in order to keep the side layer solution tractable by means of analytical methods.

The analytic solution of the 2D MHD-flow which is obtained using the methods of matched asymptotics. This method is based on the calculation of the velocity and the induced magnetic field. It yields the following result for the flow rate in the side layers Q_S for a rectangular duct which is symmetric with respect to the plane $x - z$:

$$Q_S = \frac{dp}{dx} \cdot \sqrt{2M} \sum_{j=0}^{\infty} \frac{1}{\beta_j^{7/2} \left(1 + c_S \gamma_j \sqrt{M}\right)}; \tag{2.12}$$

with $\beta_j = (j+1/2)\pi$ and $\gamma_j = \sqrt{\beta_j/2}$. The pressure gradient dp/dx behaves:

$$\frac{dp}{dx} = d\left[\frac{d\,(1+c_H)}{c_H} + \sqrt{8M}\sum_{j=0}^{\infty}\frac{1}{\beta_j^{7/2}\left(1+c_S\gamma_j\sqrt{M}\right)}\right]^{-1}, \tag{2.13}$$

where the aspect ratio of the duct d is given by $d = 2a/(2b)$, and $2b$ is the width of the duct perpendicular to B.

Three different limiting cases should be outlined:

- If $c_S \gg 1/\sqrt{M}$, which is known as *core–flow–approximation* (see Molokov&Bühler 1994), equation 2.13 asymptotes to the well known pressure gradient formula:

  $$\frac{dp}{dx} = \frac{1}{\left(1+\frac{1}{c_H}+\frac{2}{3dc_S}\right)}. \tag{2.14}$$

  Since it is often necessary to check in the numerical codes the flow rate carried by the side layers is given here analytically by:

  $$Q_S = \frac{1}{\left[3\cdot c_S\cdot\left(1+\frac{1}{c_H}\right)+\frac{2}{d}\right]}. \tag{2.15}$$

- From equation 2.14 it is clear that if $c_S \rightarrow 0$ the *core – flow – approximation* is not longer valid. Instead for $c_S = 0$ the following pressure drop relation is obtained

  $$\frac{dp}{dx} = \frac{d\cdot c_H}{\left(d+2\varsigma c_H\sqrt{M}\right)}, \tag{2.16}$$

  where $\varsigma = 0.299$.

- If in addition the Hartmann walls are much better conductors than the side layers ($\sqrt{M}\cdot c_H \gg 1$) the resistance for the electric current is mainly determined by the side layer and the pressure gradient correlation reduces to the formula given by Hunt (1965),

  $$\frac{dp}{dx} = \frac{d}{2\sqrt{M}\varsigma}. \tag{2.17}$$

  This means that for this specific case the pressure gradient is independent of c_H and the Hartmann walls act like perfect conductors. Additionally, the core velocity is of $O(M^{-1/2})$ and the side layers carry all volume flux.

2.2.2 Numerical analysis

The calculation of the heat transfer in a laminar MHD flow has been performed completely three-dimensional with the *FIDAP* program package using the analytically evaluated MHD-velocity profile as an input. Due to the rather thin MHD boundary layers a non-equidistant mesh has been generated in the yz-plane, see figure 1a,

whereas the grid in flow direction is equidistant. The number of grid points per unit length used in the coordinate direction x, y and z of the fluid domain are 16, 32 and 16.
Since the heat conductivity of stainless steel and the fluid is of similar magnitude, heat can be transported within the wall in flow direction and opposite to it. In the experimental setup the ratio is $\lambda_{steel}/\lambda_{NaK} = 0.684$. Due to this $O(1)$ value the fluid is especially heated upstream by the upstream heat diffusion within the wall. Therefore, the temperature in the plane $x = 0$ is not zero especially for low Pe and Re numbers. This leads to the following two consequences:

- The computations are not limited to the heated area $0 \leqq x \leqq 12.5$. They are extended to negative x-direction as well as to $x \geqq 12.5$. In order to restrict the calculation time the chosen computational domain is $-3 \leqq x \leqq 15.5$.
- Since the wall contributes also to the heat conducted in all directions the wall has to be integrated in the calculation. The discritisation of the mesh in x and y direction is the same as for the fluid domain. In $z-$direction however, three equidistant spaced grid points are used.

Because the laminar MHD velocity profile is used as input, only the energy equation (2.2) has to be solved for both the solid and the liquid domain.
In order to compare the heat transfer characteristics of the MHD flow with that of an ordinary hydrodynamic flow, reference calculations have been performed for the hydrodynamic laminar and turbulent flow. Both calculations have been performed also completely three-dimensionally but now using an equidistant mesh. Both, the laminar and the turbulent flow calculation has been performed for the whole test section length, i.e. for $-16.7 \leq x \leq 30$. Due to the restricted storage capacity of the used work station (about 125MB RAM) the flow domain has been split-up into three parts, which overlap each other by two characteristic lengths a. As inlet condition for the test part (flow domain 2) from $-3 \leq x \leq 15.5$ the results obtained for flow domain 1 are used; the same holds for flow domain 3.

Consider first the laminar flow:
The flow is assumed to be of slug flow type at $x = -16.7$. The dimensionless temperature there was chosen to be zero. The non-slip condition is applied at all walls and all walls except for the heated regions have been assumed to be adiabatic.

In the turbulent OHD flow the situation is more complicated. The calculation presented for the turbulent OHD-flow is based on the $k - \varepsilon -$ *turbulence model*, which is described in appendix A briefly.

Chapter 3

Experimental setup

The experiments have been performed in the MEKKA-facility of the Forschungszentrum Karlsruhe. Here only a brief overview of the experimental facility is given. A more detailed description may be taken from Barleon et al. (1996).
The magnet used in the experiment is a normal conducting water-cooled magnet with a maximum magnetic field strength of 2.0 Tesla. The rectangular gap has the dimensions $168mm \times 480mm$. The test section has been located in such a way that the magnetic field strength shows deviations of less than 1% along the test section of interest. The mapping of the absolute magnetic induction of the field in the plane $y = 0$ is shown in figure 3-1.

A centrifugal pump with a pressure head of 0.9MPa at a flow rate of $22m^3/h$ circulates the eutectic sodium-potassium alloy $Na^{22}K^{78}$ (melting point -11°C) at temperatures below 250°C. The thermophysical properties of this alloy have been described in detail by O'Donell et al. (1989). In the investigated temperature range ($T \approx 50°C$) NaK has a Prandtl number of $Pr = 0.024$. An additional electromagnetic pump is used for the high temperature wetting procedures above 250°C and also for very low flow rates. During a wetting procedure at $350°C$ impurities on the steel surface, such as oxygen or alloy components are dissolved in the NaK and extracted by cold traps. With this procedure a perfect electrical contact between the structural material and the fluid without contact resistance is ensured.
The dissipated energy is removed by an oil-cooled double tube heat exchanger. The flow rate is measured simultaneously by a gyrostatic mass flow meter and by an electromagnetic flow meter in order to have two independent measurement principles. Both agreed throughout the measurements with an accuracy of 0.5%. The entire loop can be moved on rails together with the test section along the axis of the magnet.

The test channel has a rectangular cross-section with an aspect ratio 2 : 1 and a

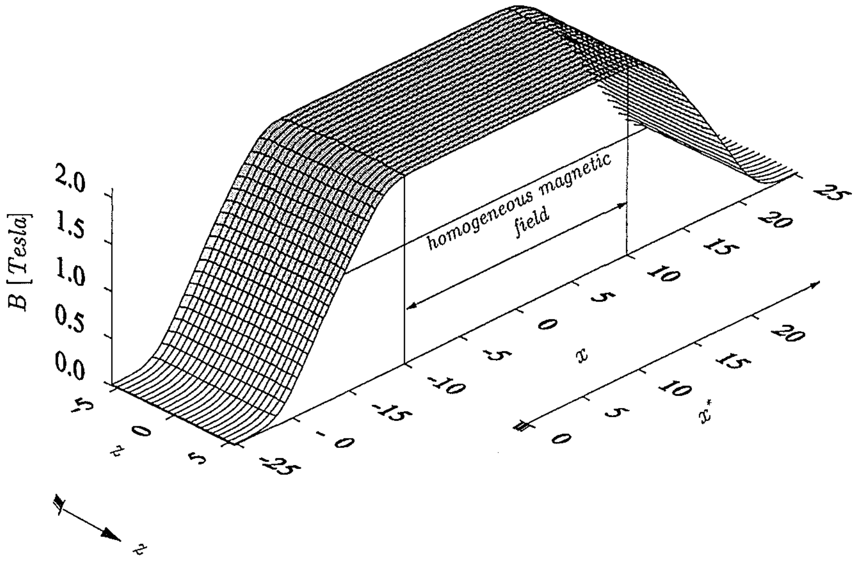

Figure 3-1 Magnetic field distribution of the magnet in the plane $y = 0$. The magnetic field strength B is given in Tesla and $\Delta B = 0.1 Tesla$.

characteristic length a of 40mm. A sketch with all dimensions scaled with a is shown in figure 1-1. All walls consist of stainless steel, which are welded by electron beam welding. The Hartmann walls, being perpendicular to B, are 1mm thick corresponding to a wall conductance ratio c_H of $c_H = 0.0119$, whereas the side walls being aligned with B, consist of 6mm thick plates which yields to $c_s = 0.0714$.

Twelve thermocouples are embedded in the side wall in groves directly at the fluid-wall interface at three different axial positions, namely at the entrance of the heater ($S1$ at $x = 0$), in the middle of the heated section ($S2$ at $x = 6.25$) and also at the outlet of the heated section ($S3$ at $x = 12.5$). These thermocouples are counted as an array $T_{mn,i}$, where the first index denotes the axial position in x-direction ($S1$, $S2$ or $S3$). The second index n specifies the location in y-direction $(1, 2, 3$ or $4)$ and the subscript $'i'$ indicates a sensor at the fluid-wall interface.

A similar set of 12 thermocouples is embedded in the side walls at the outside facing the radiation heater. The numbering is analogous to the fluid-wall thermocouples with the exception of the index $'o'$ instead of $'i'$ indicating that these sensors are located at the outside. The exact spatial location and the definition of the indices may be taken from figure 3-2a. All thermocouples have an outer diameter of 0.5mm and are made of the pairing copper-constantan. Because for this combination the Nernst-Ettingshausen effect remains small, see Kollie et al. (1977).

The heat flux is produced by a radiation heater consisting of 5 heating rods each having an active length of 500mm and being powered by $2kW$. The heater is capable attaining a maximum heat flux of $25W/cm^2$. A sketch of the heater and its installation on the test section is shown in figure 3-2b. The heat flux is determined both by measuring the electrical power input and subtracting the heat losses and by a heat balance between inlet and outlet of the test section. In order to determine the average inlet and outlet temperatures at both ends a copper integrator has been

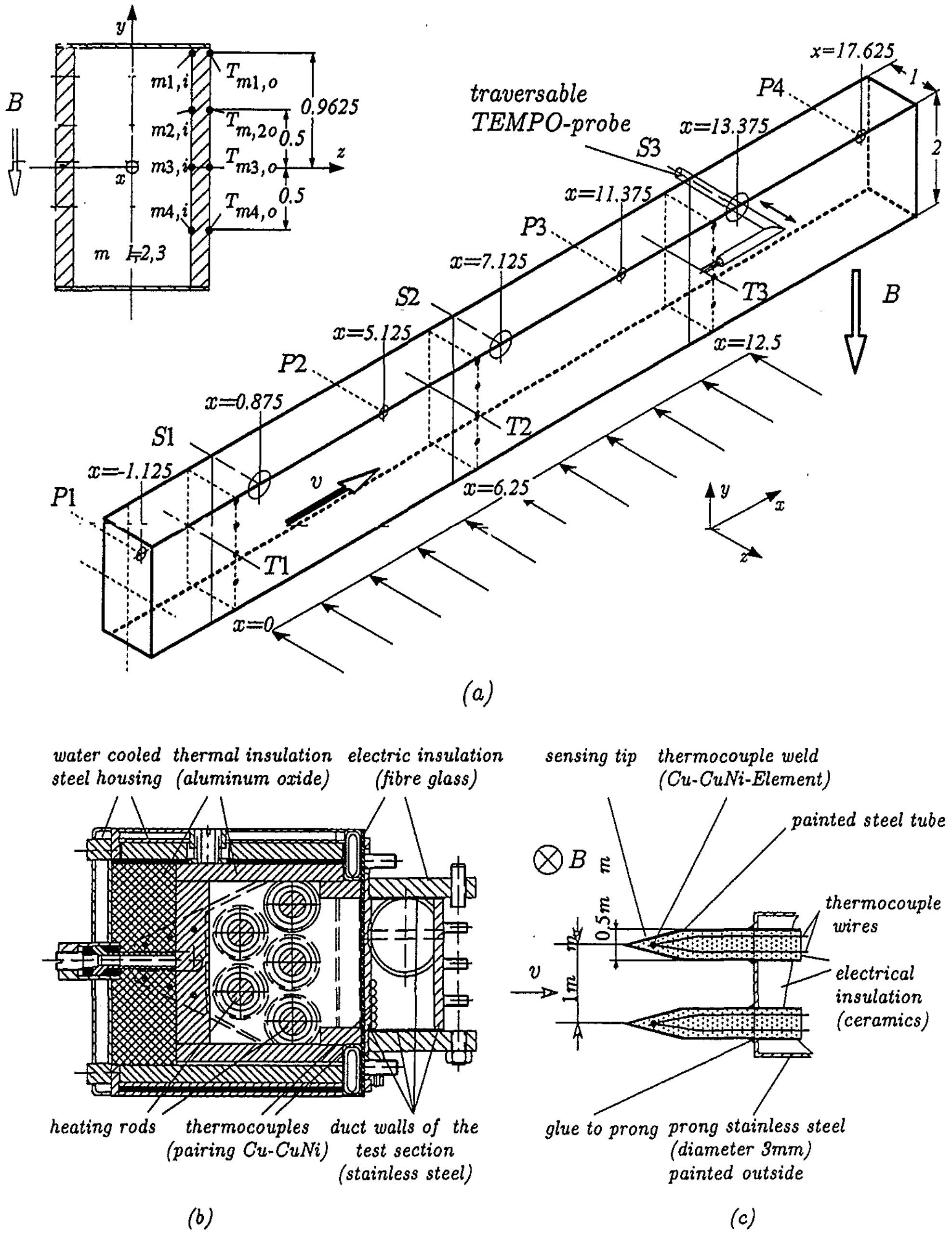

Figure 3-2 a) Geometry and location of the measurement positions of the test section. Pressure tabs are indicated with $'P'$; the thermocouples imbedded at the fluid-wall-interface are marked by $'i'$. The TEMPO probe is traversed in the plane $y = 0$ at $S1$ $(x = 0)$, $S2$ and $S3$. b.) Cut through the radiation heater with the attached test section. c.) Sketch of the TEMPO probe.

used. Within these copper integrators, through which the whole fluid flows, three thermocouples are distributed over the cross section. In order to keep the heat losses small the whole test section has been thermally insulated. Due to this very effective insulation the heat losses of the test section are negligibly small.

In the side walls at three different locations pressure taps with an inner diameter of 2mm are installed. The pressure taps are named by Pi, where $'i'$ specifies the measurement position in x-direction as the figure 3-2a shows.

In order to measure both velocity and temperature distribution in streamwise direction in the plane $y = 0$, a combined temperature-potential probe (TEMPO) has been used. The probe is traversed by a stepping motor. The probe shaft has a diameter of 3mm and is electrically insulated by a painting. The two sensing tips have distances of 1mm from each other and their steel housing has an outer diameter of 0.5mm. Within the steel tubes an electrically insulated Cu-CuNi thermocouple is embedded in order to measure the local temperature. A sketch of the TEMPO probe is shown in figure 3-2c.

Chapter 4

Results and Discussion

Within this chapter the experimental results are presented and compared with the numerical calculations. This section is organized as follows:
First, the isothermal MHD-flow is discussed and afterwards the heat transfer aspects. The subchapters deal first with the integral quantities like mean pressure which can be measured without introducing a probe in the fluid. Afterwards, the velocity distributions are discussed in dependence on the governing parameters Re, M and N. Within the presentation of the velocity field, the stability of the MHD-flow as well as the turbulence characteristics is discussed, since the kinematics of the flow field determines the heat transfer. Finally, the temperature distribution within the duct and the temperature at the fluid-wall interface are investigated.

4.1 The isothermal flow

4.1.1 The pressure distribution

For engineering purposes the pressure losses within the piping network of a heat transfer unit network are of major importance. In MHD flows with $M \gg 1$ the pressure losses depend mainly on the Hartmann number M. For high magnetic fields ($M \gg 1$) it is known from a number of experiments (e.g. Branover (1986), Kirillov et al. (1995), Stieglitz et al. (1996), Stieglitz&Molokov (1997)) that the pressure drop scaled with the electromagnetic pressure ($a\sigma v_0 B_0^2$) is even independent of the interaction parameter N. If we scale the pressure with the dynamic pressure ($p = p/(\rho u^2)$) the pressure gradient in a MHD flow at high M is proportional to $\Delta p \sim 1/v_0$.

In figure 4-1 the dimensionless pressure gradient ($\nabla p = dp/dx$) scaled with the electromagnetic pressure for the MHD duct flow in a Hartmann number range of $611 \leq M \leq 4954$ is shown as a function of the interaction parameter N. For $N \gg 1$ the measured pressure gradients nearly coincide with the calculated ones. The deviations between the measurements and the analytical solution are in a range of approximately 5%. At high Hartmann numbers, i.e. $M \geq 10^3$, the dimensionless pressure gradient remains constant in the whole range of investigated interaction parameters.

At a Hartmann number of $M = 10^3$ and interaction parameters less than 60 the pressure distribution leaves the domain where the flow is dominated by electromagnetic forces. In this low interaction parameter range the viscous dissipation starts to compete with the Joules dissipation, which is expressed by an increasing pressure gradient. The figure 4-1 demonstrates that the inertialess range, which is only governed by electromagnetic-viscous interaction, is shifted towards higher N as the Hartmann number decreases.

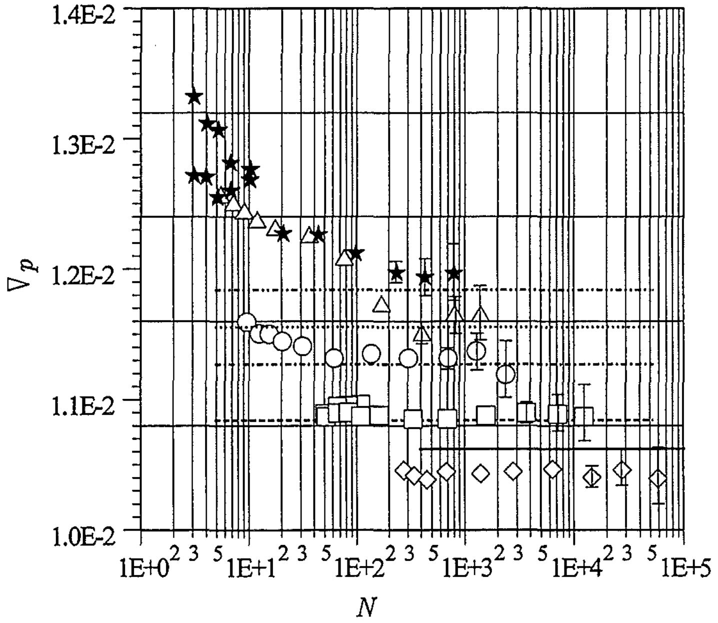

Figure 4-1 Measured pressure gradient ∇p as a function of the interaction parameter N for different Hartmann numbers $611 \leq M \leq 4954$. The lines indicate the analytically calculated values. (◇, –) $M = 4954$; (□, – – –) $M = 2453$; (○, – · –) $M = 1069$; (△, · · ··) $M = 800$; (★, – · · – ··) $M = 611$.

The flow domain in which inertia, viscosity and electromagnetic effects balance each other is highly non-linear, compare Molokov et al. (1994), and can be described by the following equation.

$$\frac{1}{M^2}\frac{d^2 v}{dx^2} + j \times B = -\nabla p + \frac{1}{N}(v \cdot \nabla)\, v. \tag{4.1}$$

As the Hartmann number is further decreased down to values of $M \approx 74$ the inertialess flow domain can not be found in the experiment, see figure 4-2. The reason is that in the high interaction parameter range the pressure decreases to values which can not be resolved by the used pressure transducers.

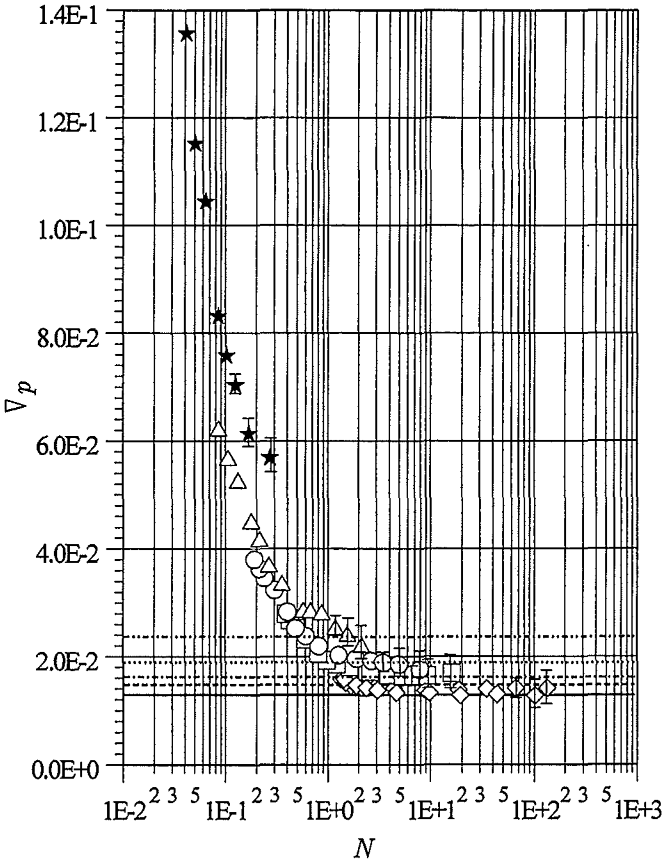

Figure 4-2 Measured pressure gradient ∇p as a function of the interaction parameter N for different Hartmann numbers $74 \leq M \leq 411$. The lines indicate the analytically calculated values. (◇, —) $M = 410$; (□, – – –) $M = 224$; (○, – · –) $M = 150$; (△, · · · ·) $M = 103$; (★, – · · · – · ·) $M = 74$.

From an engineering point of view it is interesting to find the transition point between MHD and OHD. In OHD, the pressure drop in a piping is expressed by the friction parameter λ which is defined by

$$\lambda = \frac{\Delta p}{\frac{\varrho}{2}\overline{u}^2} \frac{D_H}{L} \frac{1}{f}, \tag{4.2}$$

where D_H is the hydraulic diameter given by the relation

$$D_H = \frac{4 \cdot Area}{circumferrential\ length}. \tag{4.3}$$

Herein, L is the length over which the pressure difference Δp is measured and f is a form factor, which takes into account the aspect ratio of the duct. For the duct investigated f is 0.922 in the laminar flow regime and $f = 1$ in the turbulent flow, see Zierep&Bühler (1991). For laminar OHD flows, λ is given by the Poiseuille relation $\lambda = 64 \cdot f/Re$,whereas in turbulent flows different relations valid for the different Reynolds number regimes appear see equations 4.4 and 4.5

$$\lambda = \frac{0.3164}{\sqrt[4]{Re}} \text{ for } \left(2320 < Re < 10^5\right); \tag{4.4}$$

$$\frac{1}{\lambda} = 2\lg\left(Re\sqrt{\lambda} - 0.8\right) \text{ for } \left(10^5 < Re < 3 \cdot 10^6\right). \tag{4.5}$$

Relation 4.4 is called the Blasius Relation, where in the literature the implicit equation 4.5 is called Prandtl Equation.

From the pressure drop relations of MHD controlled flow, see eq. 2.13, and the OHD controlled flow the power laws for the friction coefficient λ as a function of the hydraulic Reynolds number can be easily deduced. In pure MHD controlled flows as well as in laminar OHD flow the friction coefficient λ scales with $\lambda \sim Re^{-1}$. In a turbulent OHD flow in the Blasius regime the friction coefficient scales with $\lambda \sim Re^{-7/4}$.

In figure 4-3 the friction coefficient λ is drawn as a function of the Reynolds number for different Hartmann numbers. The figure shows that with increasing Re the friction coefficient tends towards the values calculated for turbulent OHD flows. For a Hartmann number of $M = 103$ and Reynolds numbers $Re \geq 10^5$ the pressure drop for a MHD flow coincides exactly with the one of a turbulent hydraulic flow.

If the Hartmann number is further decreased down to about $M \approx 50$, the transition Reynolds number, at which the pressure drop of MHD and pure OHD controlled flows meat each other, decreases. In figure 4-4 the friction parameter λ is shown as a function of the Reynolds number for a successive decrease of M. The measurements could not be continued to smaller Hartmann numbers than $M \approx 50$ because of the resolution of the pressure transducers. For the transition Reynolds number in the measured range of parameters the following fit is obtained:

$$Re_{transition} \approx 100 \cdot M. \tag{4.6}$$

Of course, from a physical point of view the transition Reynolds number must depend on M, because the magnetic field strength determines both the velocity profile and the current density causing the pressure drop. The proportionality factor in equation (4.6) of 100 found in the experiment must depend on the wall conduction ratios of the duct.

However, in this context it should be emphasized that only the friction coefficient λ of a MHD flow ($M > 0$) is the same as the one of the OHD flows. But the flow structure or, more explicitly, the turbulence structure within the eddies of a turbulent flow may be completely different between OHD and MHD.

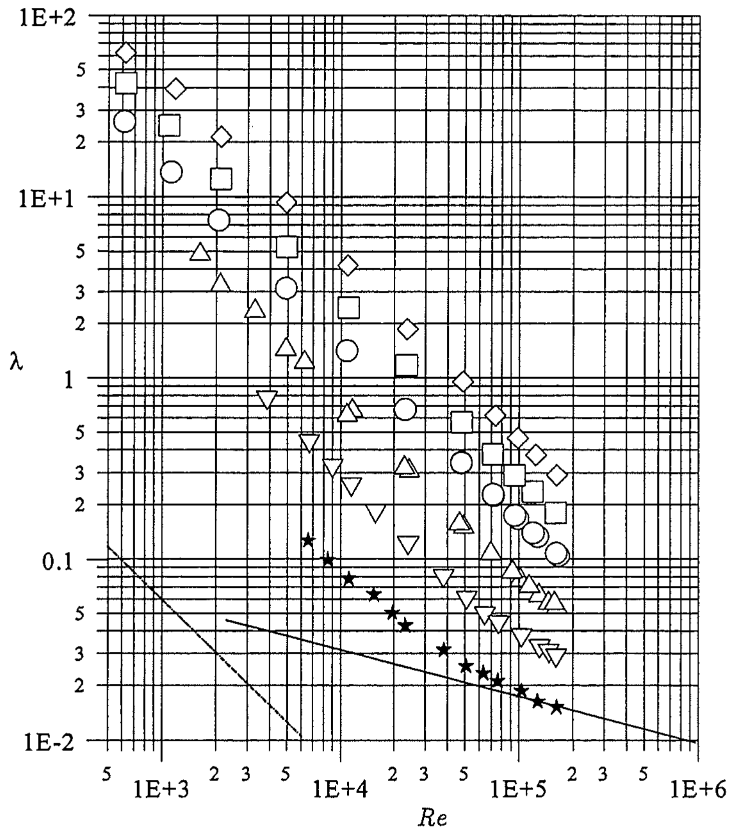

Figure 4-3 Measured friction coefficient λ as a function of the Reynolds number Re. (◇) $M = 1069$; (□) $M = 800$; (○) $M = 611$; (△) $M = 410$; (▽) $M = 224$; (★) $M = 103$; (—) Blasius relation; (– · –) laminar OHD flow.

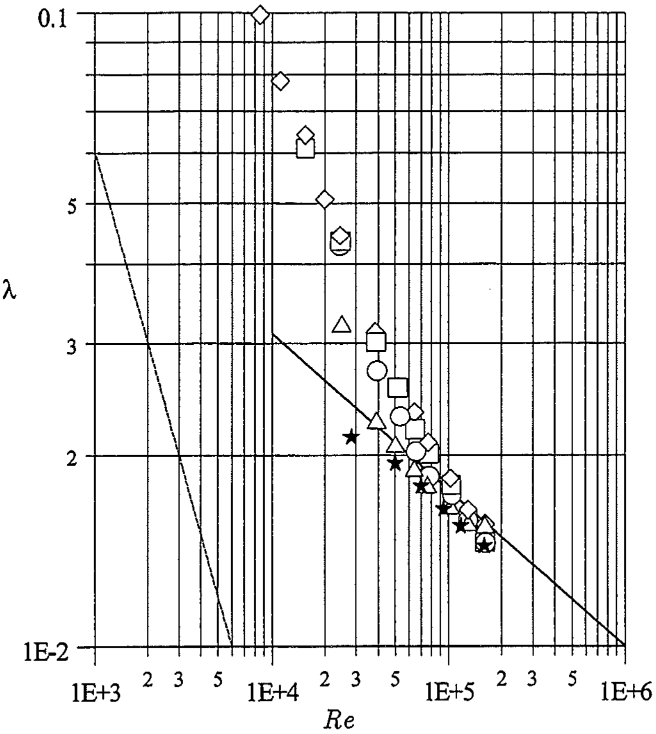

Figure 4-4 Measured friction coefficient λ as a function of the Reynolds number Re. The lines indicate the relations known in OHD. (◇) $M = 103$; (□) $M = 84$; (○) $M = 74$; (△) $M = 52$; (★) $M = 0$; (—) Blasius relation; (– –) laminar OHD flow.

4.1.2 The velocity distribution

All velocity profiles shown in this subsection have been recorded in the plane $y = 0$ with the TEMPO-probe. The probe is traversed in $z-$direction from $-0.4 \leq z \leq 0.45$.

In the first measurements the location of the probe in $x-$direction is varied in order to study the influence of the developing length. The coordinate $x^* = 0$ marks the beginning of the region, where the magnetic field deviates less than 1% from the constant field.

In figure 4-5 the time averaged velocity in streamwise direction is shown as a function of z for different x^* and the same set of parameters M, N. The core-velocity measured for each x^*-position coincides nearly exact with the analytically calculated value. Nevertheless, the velocity profile changes slightly in x^*- direction. The width of the side layer observed experimentally at each x^*-location is larger than the width calculated for a fully developed two-dimensional MHD flow. Moreover, as the flow proceeds in x^*-direction the side layer width seems to grow. This effect is most clearly expressed in the local velocity minimum of the side layer jet. This minimum moves towards the duct centre as x^* increases.

In figure 4-6 the local minimum of the velocity near the wall is shown as a function of x^*. The position at which this minimum appears, further named δ_d, obeys approximately to the power law $\delta_d \sim x^{*-0.32}$. The exponent found in the experiment is close to the value $-1/3$ which has been also been detected in inertial flows in previous experiments, see Stieglitz et al. (1995). This results indicate that the flow is not fully

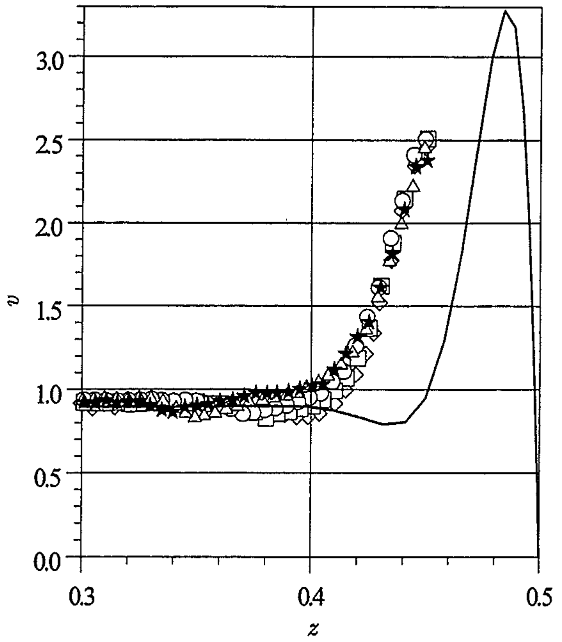

Figure 4-5 Streamwise velocity v in the plane $y = 0$ as a function of the lateral coordinate z for different x^*. Boundary conditions: $M = 4797$, $N = 1604$, $Re = 17808$. (◇) $x^* = 4.0$; (□) $x^* = 7.125$; (○) $x^* = 10.25$; (△) $x^* = 13.375$; (★) $x^* = 16.25$; (—) calculation fully developed flow.

developed even for more than 16 characteristic length after entering the homogeneous field.

It also demonstrates that only pressure measurements for determining the fully developed flow may lead to misleading results. Nevertheless, since the changes in the flow profile are not essential for $x^* > 4$ in the subsequent sections the flow is assumed hydraulically developed.

The velocity profiles being discussed in the following have all been recorded at $x = 12$ or in terms of x^* at $x^* = 16.25$ in the plane $y = 0$. First, the velocity profiles for the highest Hartmann number ($M = 4840$) are discussed.

In figure 4-7a the velocity is shown as a function of z for different interaction parameters N. The core velocity found in the experiments at all interaction parameters agrees within 2% with the analytically calculated values. Moreover, also the inflection type velocity profile at the transition of the core flow matching the side layer is found. Nevertheless, the local minimum of the velocity in the experiments is not located at the same position as calculated by the analytical solution. Even for the highest interaction parameters measured ($N = 12248$) the velocity minimum is shifted towards the duct centre. This experimental result coincides with the observations of Reed and Picologlou (1989). However, with gradually decreasing Reynolds numbers the local velocity minimum moves only slowly towards the analytically calculated position. The magnitudes of the velocity extrema, i.e. peak velocity of the jet and local velocity minimum, found in the experiment agree rather well with the analytical solution. Unfortunately, for the highest Hartmann number investigated the decay of

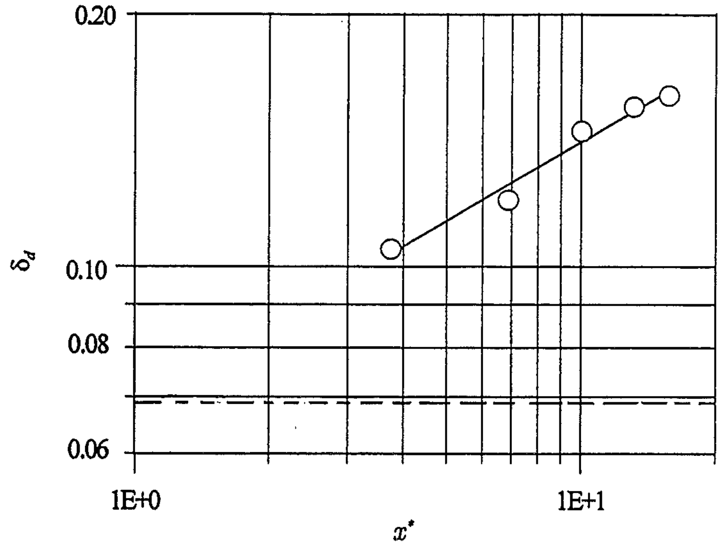

Figure 4-6 Distance of the local velocity minimum from the wall δ_d as a function of x^* for $M = 4797$, $N = 1604$ and $Re = 17808$. (○) measurement; (—) fit; (— —) calculation fully developed flow.

the velocity towards the wall could not be measured because the width of the side layer at this high M is smaller than resolution of the probe (i.e. distance between the sensing tips of the probe).

For $N \geq 3454$ ($Re \leq 7.5 \cdot 10^3$) the shape of the velocity profile alters only marginally with N (Re). The flow in this Reynolds number regime is laminar both in the side layer and the core, see §4.1.3 stability. As the Reynolds number is increased further the side layer width increases, because the side layer is turbulent in that Reynolds number regime.

For $Re \leq 1.8 \cdot 10^4$ the shapes of the velocity profiles are similar to the laminar profiles, because the turbulence intensity is quite low. Thus, the turbulent deviations of the velocity does not contribute significantly to the mean velocity profile.

As the Reynolds number exceeds $Re = 1.8 \cdot 10^4$ the side layer is stretched further, see figure 4-8. The width of the side layer thickness δ_s as a function of the Reynolds number is shown in figure 4-7b. In this Reynolds number regime also the shape of the side layer velocity profile is modified due to the turbulent velocity oscillations. The quite large velocity fluctuations expressed by a turbulence intensity Tu of up to $Tu \approx 0.2$ fills up the local velocity minimum in the side layer. For $Re = 7.4 \cdot 10^4$ the velocity minimum almost diminishs. The structure of the turbulence developing in time-dependent MHD-flows will be briefly discussed in §4.1.3. A more detailed analysis is given in the report of Burr (1997).The side layer stretching as a function of the Reynolds number is also found in the calculations of Cuevas et al. (1996, 1997). But, the shape of the velocity profiles calculated differs to the experiment. The major differences occur especially in the transition region of core to side layer. Unfortunately, the scaling of the side layer thickness with the Reynolds number is not calculated.

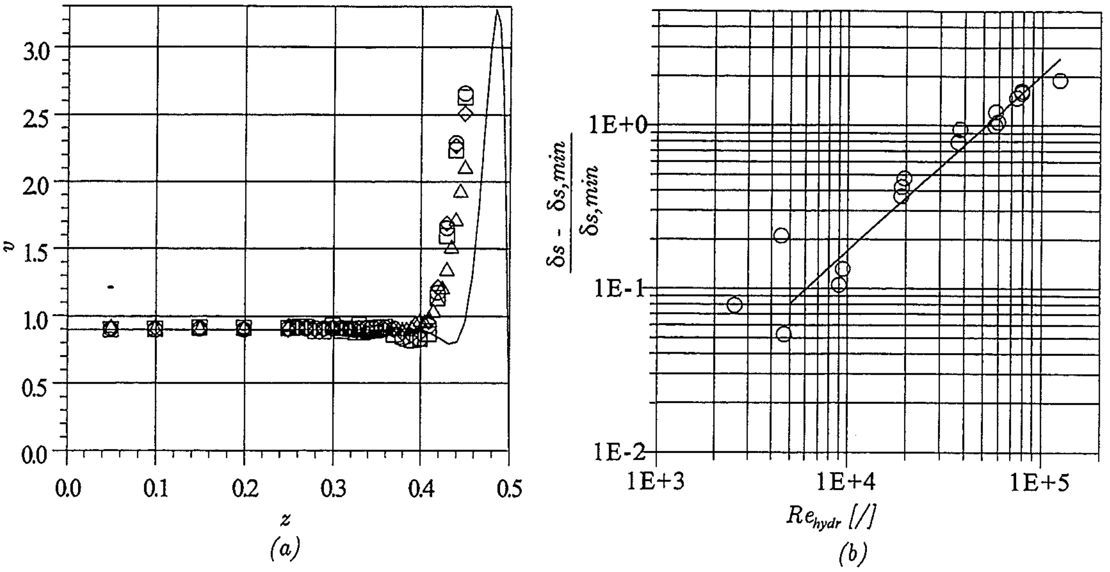

Figure 4-7 a.) Streamwise velocity v in the plane $y = 0$ as a function of z for different N at $M = 4840$.(◇) $N = 12248$ ($Re = 2550$); (□) $N = 6947$ ($Re = 4496$); (○) $N = 3454$ ($Re = 9043$); (△) $N = 1649$ ($Re = 18943$); (–) calculation fully developed flow.

b.) Relative width of the side layer as a function of the Reynolds number Re. The solid line represents a fit through experimental data and obeys $(\delta_S - \delta_{S,min})/\delta_{S,min} \sim Re^1$.

The thickening of the side layer is caused by electromagnetic-inertial interaction. In contrast to other MHD-flow phenomena, where the flow is governed by electromagnetic-inertial interaction -see theoretical work of Hunt&Leibovich (1967) and Cuevas et. al (1996,1997) and experiments by Stieglitz et al. (1996)- the relative growth of the side layer thickness δ_S scales here approximately with Re^1. A side layer thickening has been also measured in the experiment of Reed&Picologlou (1989).
The values presented up to now are the time averaged values. The potential gradient between the two tips of the probe, which is proportional to the velocity, is averaged over 16 seconds. It turned out in the measurements that the flow near the inflection points of the side layers becomes unstable. The transition from steady to time dependent turbulent flow takes place if a critical Reynolds number is exceeded as it is known from shear flow instabilities in classical OHD. This topic will be discussed in the next subsection.

So far the physical aspects of the flow have been only discussed for the highest investigated Hartmann number.
As shown in §1 and in the figures 4-9a-c the velocity profile is strongly dependent on the Hartmann number. Especially the side layer width increases with decreasing Hartmann number. In figures 4-9a-c the velocities v are plotted as a function of z for three different Hartmann numbers, $M = 2420$ (a), $M = 1219$ (b) and $M = 518$ (c) and different interaction parameters N.
Figure 4-9a shows that for the highest interaction parameter at $M = 2420$ the maximum of the side layer jet is experimentally observed. However, again the width of the

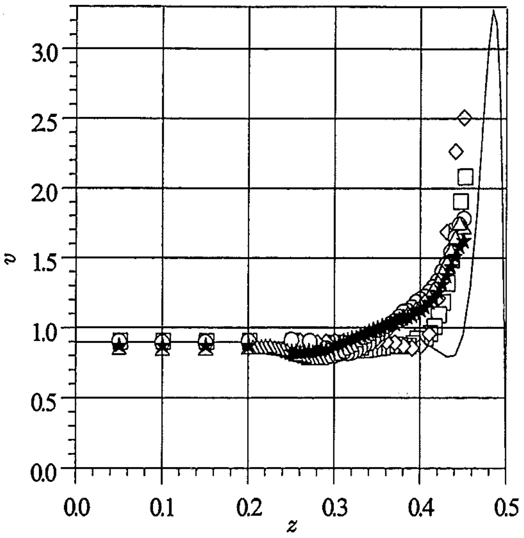

Figure 4-8 Velocity v as a function of z for different N at $M = 4840$. Legend: (◇) $N = 12248$ ($Re = 2550$); (□) $N = 1716$ ($Re = 18203$); (○) $N = 843$ ($Re = 37054$); (△) $N = 540$ ($Re = 57845$); (★) $N = 420$ ($Re = 74372$); (–) calculation fully developed flow.

side layer is larger than calculated analytically. The measured peak velocities are of the same magnitude as the calculated peak velocities. As the velocity is increased the side layer thickens but the characteristics of the profile, expressed by a local velocity minimum remains up Reynolds numbers $Re \leq 1.68 \cdot 10^4$. If the velocity is further increased (N decreasing) the velocity profile is smoothed and finally for $N = 206$ no local velocity minimum is found. The reason should be the same as detected for $M = 4840$.

The figures 4-9b and 4-9c present also the velocities as a function of z at different interaction parameters for $M = 1219$ and $M = 518$. With decreasing Hartmann numbers the agreement between measurements and analytic solution for the side layer velocities gets better. At all Hartmann numbers ($M \leq 1220$) the core velocity coincides with the calculated values.

For a Hartmann number of $M = 518$ in all measurements the velocity decay towards the side wall is resolved in the experiments. The deviations between experiment and analysis does not exceed more than 15%.

4.1.3 Stability of the MHD-flow

A view on the velocity profiles for different Hartmann numbers $M = 350 \rightarrow 4840$ (figure 4-10) reveals that the velocity gradients increase as M increases. Therefore, the onset of instabilities is likely expected for higher Hartmann numbers than for lower ones, because the velocity gradients $\partial v/\partial z$ increase with growing Hartmann numbers.

The aim of this report is neither the detailed investigation of the turbulence structure nor the determination of the neutral stability of the flow. Nevertheless, the turbulence

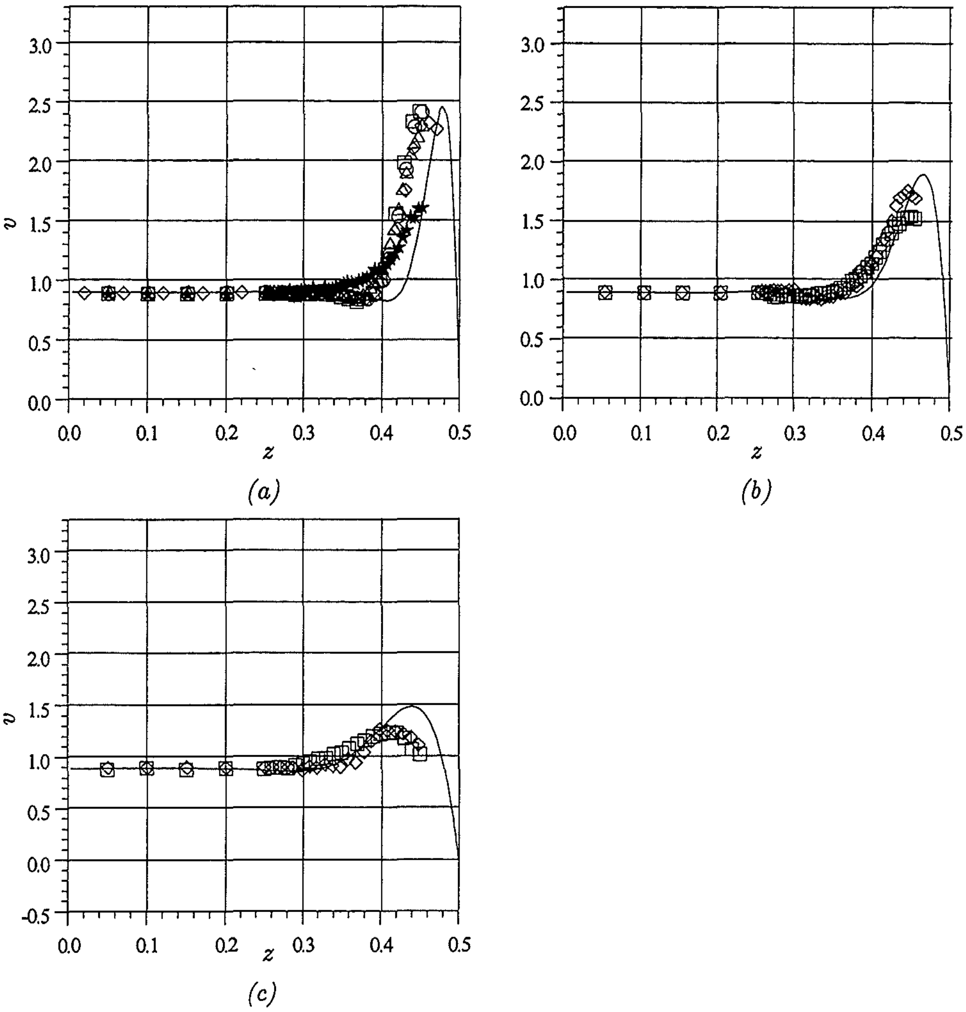

Figure 4-9 Velocity v as a function of z for different N and M.
(a) $M = 2420$: (◇) $N = 3724$ ($Re = 2097$); (□) $N = 1809$ ($Re = 4316$); (○) $N = 877$ ($Re = 8904$); (△) $N = 464$ ($Re = 18829$); (★) $N = 206$ ($Re = 37906$); (–) calculation fully developed flow.
(b) $M = 1219$: (◇) $N = 52$ ($Re = 38101$); (□) $N = 26$ ($Re = 76202$); (–) calculation fully developed flow. (c) $M = 518$: (◇) $N = 95$ ($Re = 3766$); (□) $N = 16$ ($Re = 22360$); (–) calculation fully developed flow.

intensity of the flow has been recorded and a sensitivity study on the stability of the velocity profile in main flow direction has been performed.
The turbulence intensity Tu, which is defined as

$$Tu = \frac{\sqrt{\left(\overline{u'^2}\right)}}{\overline{u}}. \tag{4.7}$$

It is built like in OHD (, see e.g. Zierep (1982)) and is a measure of the magnitude of the fluctuations compared to the mean flow.

In figure 4-11 the turbulence intensity is plotted versus the $z-$coordinate for several interaction parameters at a Hartmann number $M = 4840$.
For $N > 3439$ ($Re < 8372$) no fluctuations of the velocity in streamwise direction are observed. At $M = 4840$ and $N = 3439$ the first fluctuations were recorded at the $z-$position were the highest velocity gradient ($z = 0.4$) in mean flow direction appears. At all other measurement positions, however, the flow remains laminar and the turbulence intensity measured there ($Tu \approx 2\%$) is the background noise of the system. It exists one maximum of the turbulence intensity Tu. At the second inflection point of the velocity profile the shear stress is not so high that it leads to a measurable creation of vortices.
If the velocity is further increased the turbulence intensity increases, too. Moreover, an additional maximum of the turbulence intensity appears. It is marked for the curve □ ($N = 1.723 \cdot 10^3$) in figure 4-11 by the large circle.
A Fourier-transform of the streamwise velocity fluctuations at two different $z-$locations of the duct gives an explanation of the appearance of two peaks in the turbulence intensity. In the figures 4-12a, b the Fourier transforms of the probe signals are shown as a function of the frequency f for two different positions $z = 0.35$ and $z = 0.45$ and for a Hartmann number of $M = 4840$ and an interaction parameter of $N = 843$. At both positions the characteristic frequency of the signal is about 20 Hz and the shape of the frequency spectrum is similar. A detailed analysis of the time dependent signal reveals, that the peak appearing at $z = 0.35$ is directed in negative streamwise direction. As a consequence of this analysis some conclusions on the geometrical shape of the vortices can be drawn. The vortices are detaching from the side layer, where the highest velocity gradients appear and they are rotating counterclockwise. In a more detailed study by Burr (1997) this shape of the vortex is verified. He used a four pole probe, which is capable to measure also the spanwise velocity component.

At even lower N (higher velocities), i.e. for $N \leq 10^3$, the relatively sharp second extremum of the turbulence intensity disappears. At these lower interaction parameters a large region with a high turbulence intensity appears. The reason is that the turbulence structure is not as defined as at lower velocities and vortices of different shape and rotation velocity detach from the side layer. Thus, a broader region of high turbulence intensity is formed. If N is further decreased the domain of high turbulence intensity grows. The growth in $z-$direction corresponds to the growth of the side layer as shown in figure 4-8. This region of high turbulence intensity may be the reason why the velocity gradients in the side layer in the time averaged signals previously discussed gets weaker for low interaction parameters. In any case the

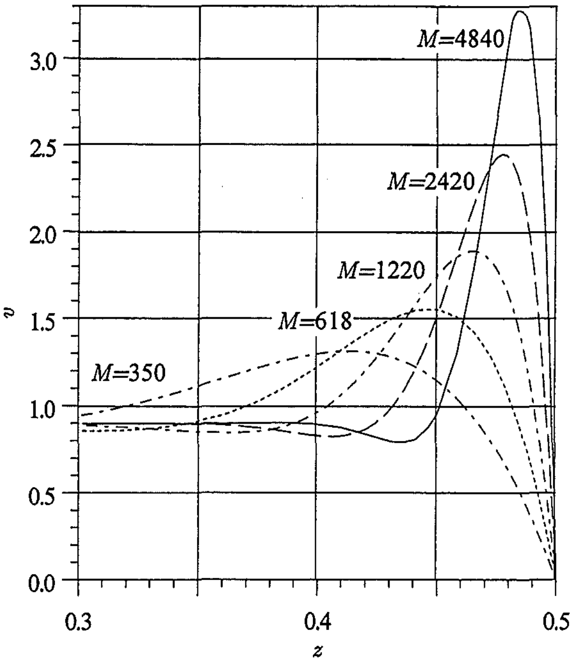

Figure 4-10 Calculated velocity v as a function of z for varying Hartmann numbers M.

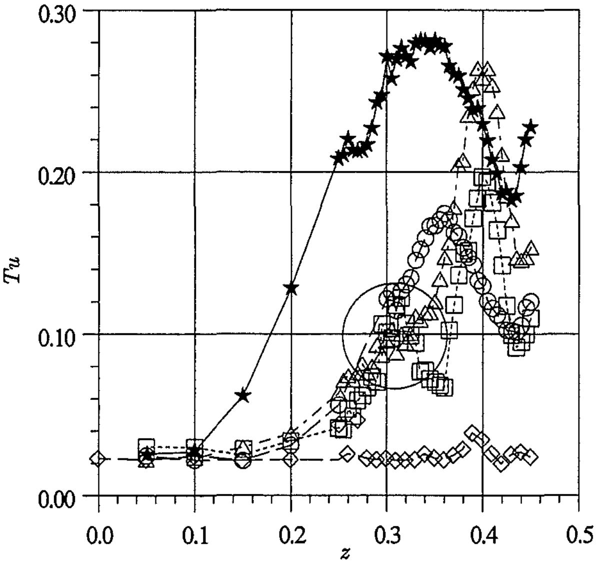

Figure 4-11 Measured turbulence intensity Tu as a function of z for different N at $M = 4840$. (◇) $N = 3439$ ($Re = 8372$); (□) $N = 1723$ ($Re = 18203$); (○) $N = 843$ ($Re = 37054$); (△) $N = 540$ ($Re = 57845$); (★) $N = 420$ ($Re = 74372$); (–) calculation fully developed flow.

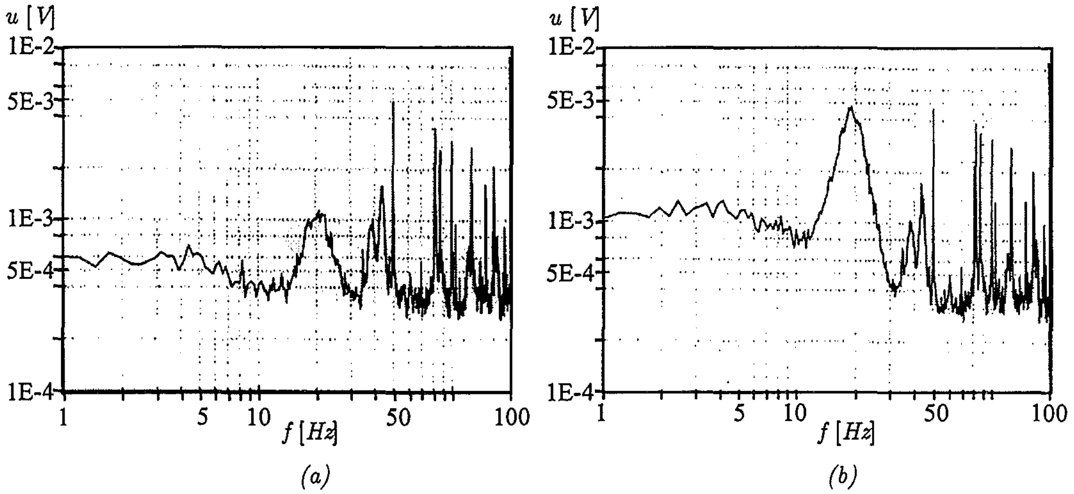

Figure 4-12 Fourier transform of the velocity signal as a function of the frequency for $M = 4840$, $N = 843$ at the positions $z = 0.35$ (a) and $z = 0.45$ (b).

high turbulence intensity is the reason for the gradual disappearance of the velocity minimum in the side layer jet.

Although the turbulence intensities found in the near wall region are quite strong the turbulence intensities in the core-flow are nearly zero. It seems that the turbulent structures produced by the MHD-shear flow do not penetrate into the core flow and there is no momentum transfer to the core flow.

Finally, let us focus our discussion on the stability of the MHD flow in dependence of the Hartmann number M. In figure 4-11 it has been demonstrated that the first instabilities occur, where the highest velocity gradients in main flow direction appear, similar like a shear flow instability in ordinary hydrodynamics.
In the book of Branover (1978b) the laminar-turbulent transition in rectangular ducts is analyzed and the following empirical formula for the laminar-turbulent transition is given:

$$Re_{crit} = (215 - 85 \cdot e^{-0.35 \cdot \beta}) \cdot M, \tag{4.8}$$

where β is the aspect ratio. This relation is valid if $M \gg 1$.For the test section investigated ($\beta = 2$) the mentioned condition gives:

$$Re_{crit} = 172.79 \cdot M. \tag{4.9}$$

However, Branover does not take into account the wall conductivity. He mentions that the wall conductivity *does not affect the stability.* Recent investigations performed by Bühler (1996) demonstrate that especially the damping of the vortices is strongly dependent on the conductivity of the Hartmann wall. A detailed analysis shows that the characteristic decay time $\tau$of a vortex in a transverse magnetic field is given by the relation:

$$\tau = \frac{1}{\left(\frac{N}{M} + \frac{c_H \cdot N}{1 + c_H}\right)}. \tag{4.10}$$

An increasing conductivity of the Hartmann wall leads therefore to shorter decay times and shifts at the same Hartmann number the laminar turbulent transition to lower interaction parameters. Thus, even an empirical correlation should take into account the conductivity c_H of the Hartmann walls.
Another attempt to define the critical Reynolds number in a MHD duct flow with electrically conducting walls has been made by Rossant (1976). He defined the critical Reynolds number to be dependent on the square root of the Hartmann number in the way:

$$Re_{crit} = K \cdot \sqrt{M}, \tag{4.11}$$

where K is a constant depending on the wall conductance ratios of the wall. However, this attempt to describe the laminar turbulent transition in the high Hartmann number range leads to results being in contradiction with the experiments of Reed and Picologlou (1989), Burr (1997) and the present experiments. The relationship 4.11 suggests that the critical Reynolds number increases with increasing Hartmann number, which is not found in the experiments at high Hartmann numbers. Nevertheless, in the lower Hartmann number range the relationship 4.11 fits the experimental data obtained in the experiment of Rossant.

The stability of the MHD side layer jet in a rectangular duct has also been investigated by means of a linear stability analysis by Ting and Walker (1991). Perturbations were applied to the analytically calculated side layer solutions. The results of neutral stability analysis were compared to an experiment of Reed and Picologlou (1989). The critical Reynolds number found in the analysis has been one order of magnitude too small and the fluctuation frequency has been by the same order too high. The reason for disagreement may be that the side layer thickness in the experiment was significantly larger than assumed in the analysis. Reed and Picologlou (1989) found that the onset of the instability is insensitive to the Hartmann number as long as $M \gg 1$. The evolution and the final state of the instability is strongly dependent on M.
This variety of partly contradictory results reveals the necessity to study this transition more carefully.

The spectral density distribution (performed by a Fourier analysis) has been measured and a first appearance of a peak merging out of the noise was taken as a begin of turbulence. This method of averaged spectra has the advantage of a definite determination of the appearance of a time dependent flow.

The neutral stability measurements in the midplane ($y = 0$) revealed the result displayed in figure 4-13. Since the shape of the side layer velocity profile is mainly determined by the Hartmann number M, the location of the first instabilities is a function of z. As detected in the present and previous experiments, the slope of the M-shaped side layer velocity profile acts as a generator of the instabilities. With

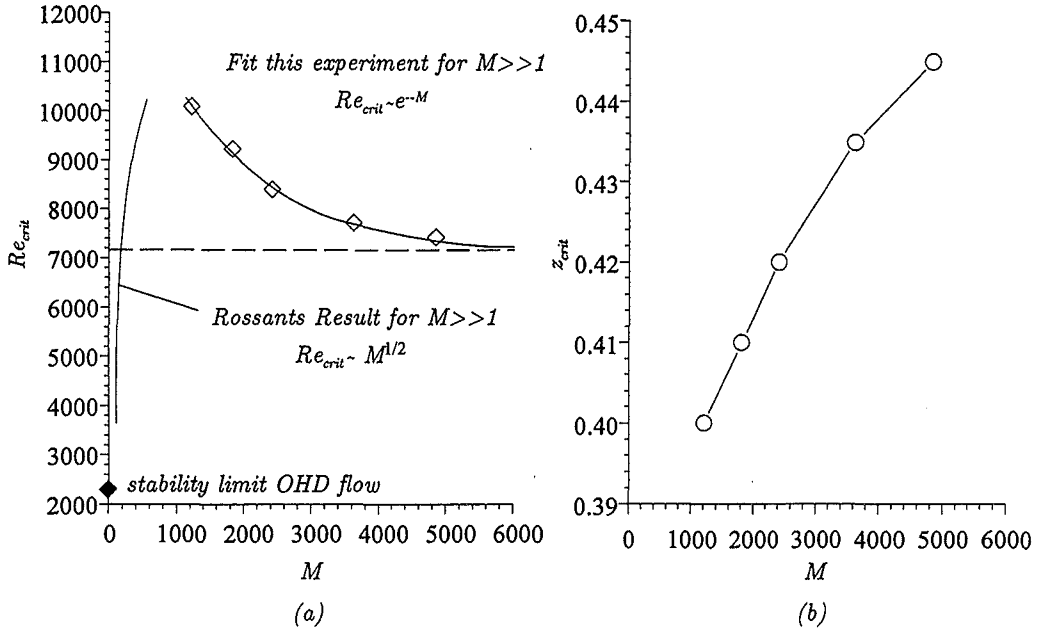

Figure 4-13 (a) Measured critical Reynolds number Re_{crit} ($\diamond$) for laminar-turbulent transition as a function of M in a rectangular duct with thin electrically conducting walls. The dotted line indicates the stability limit obtained by the exponential fit.
(b) Measured $z-$position at which smallest Re_{crit} appears as a function of M.

increasing Hartmann number the slope $\partial u/\partial z$ increases and thus the critical Reynolds number decreases. Although the generation of vortices is favored with increasing Hartmann number the Hartmann damping of the vortices at the Hartmann walls also increases with the Hartmann number. These two effects are counteracting and competing with each other. The experimentally measured critical Reynolds number is shown in figure 4-13a. With a fitting procedure based on the minimum of the least squares the following relation

$$Re_{crit} = 7150 + 2970 \cdot e^{\left(\frac{1210 - M}{1500}\right)} \tag{4.12}$$

is obtained. This relation is plotted in figure 4-13a as a solid line. Resulting from the fit the critical Reynolds number decays proportional to e^{-M} and tends for $M \longrightarrow \infty$ to $Re_{crit} = 7150$. However, in our experiment equation 4.12 is only valid for $c_H \gg 1/M$ and $M \gg 1$.

It would be worthwhile to define a stability limit of MHD duct flows in ducts with thin electrically conducting walls. As already outlined, the influencing parameters are the generation of vortices, which are determined by the steepness of the velocity profile scaling with $\sqrt{M}$, and the damping of the vortices by electromagnetic viscous dissipation scaling with the characteristic decay time of a vortex.

According to the Hartmann number dependence of the side layer velocity profile the z-position where the first instabilities occur must also depend on M. Thus with decreasing Hartmann number this position must move towards the duct center because the side layer thickens and, therefore, the position of maximum shear stress moves in the same direction. The experimental results displayed in figure 4-13b confirm this consideration.

4.2 Measurements with heat transfer

All heat transfer measurements have been performed in a measurement matrix in which the Hartmann number M is varied in four steps $M = 0$, 1197, 2417, 4993 and the Reynolds number Re in eight steps $Re \approx 2.4 \cdot 10^3$, $4.8 \cdot 10^3$, $9.5 \cdot 10^3$, $1.9 \cdot 10^4$, $3.8 \cdot 10^5$, $5.7 \cdot 10^4$, $7.9 \cdot 10^4$, $1.2 \cdot 10^5$ in order to cover the whole fusion blanket relevant parameter range.
The presented subchapters are organized as follows:
First, the velocity measurements are presented so far as they complete the picture of the isothermal flow previously presented. Furthermore, the temperature distribution within the liquid metal is discussed since it is strongly related to the turbulence structure within the fluid. Finally, the wall temperatures at the fluid/wall-interface are discussed and compared to the numerical results obtained with the model and compared to the data calculated for slug-flow, which has been assumed in design calculations for the liquid metal cooled blankets.

4.2.1 Velocity distribution

Although the velocity distribution has been measured in case of isothermal flow the measurements have been repeated for the conditions in which the test section is heated.
The experimental results for the heated wall show only marginally differences in the midplane $y = 0$ compared to the isothermal flow. Consequently, buoyant effects play no role in MHD flows with $M \gg 1$ in the Reynolds number range $Re = 2.4 \cdot 10^3 - 1.2 \cdot 10^5$ (or $Pe = 6 \cdot 10^1 - 2.88 \cdot 10^3$). Therefore, the assumption is justified that the temperature is acting as a quasi-passive scalar which has been made in the modelling.
In figures 4-14a-f the velocity profiles for the investigated Hartmann numbers ($1197 \leq M \leq 4993$) and Reynolds numbers are displayed as a function of z.
The figures show that at each investigated Hartmann number the velocity profiles are modified with decreasing interaction parameters. As N decreases the side layer width grows and also the local velocity minimum is shifted towards the duct centre. The increase of the velocity therefore leads to a smoothing of the profile.
The turbulence intensity is coupled to the shape of the velocity profile. Since the deviations in the velocity profiles between the isothermal and the non-isothermal flows are negligibly small also the turbulence intensities measured show the same behavior. The turbulence intensity is responsible for the momentum transfer within the fluid and thus it determines the heat flux transported.
Due to this aspect we discuss the measured turbulence intensity distribution in context with the temperature distribution within the liquid, in order to explain the heat transfer mechanisms within the fluid.

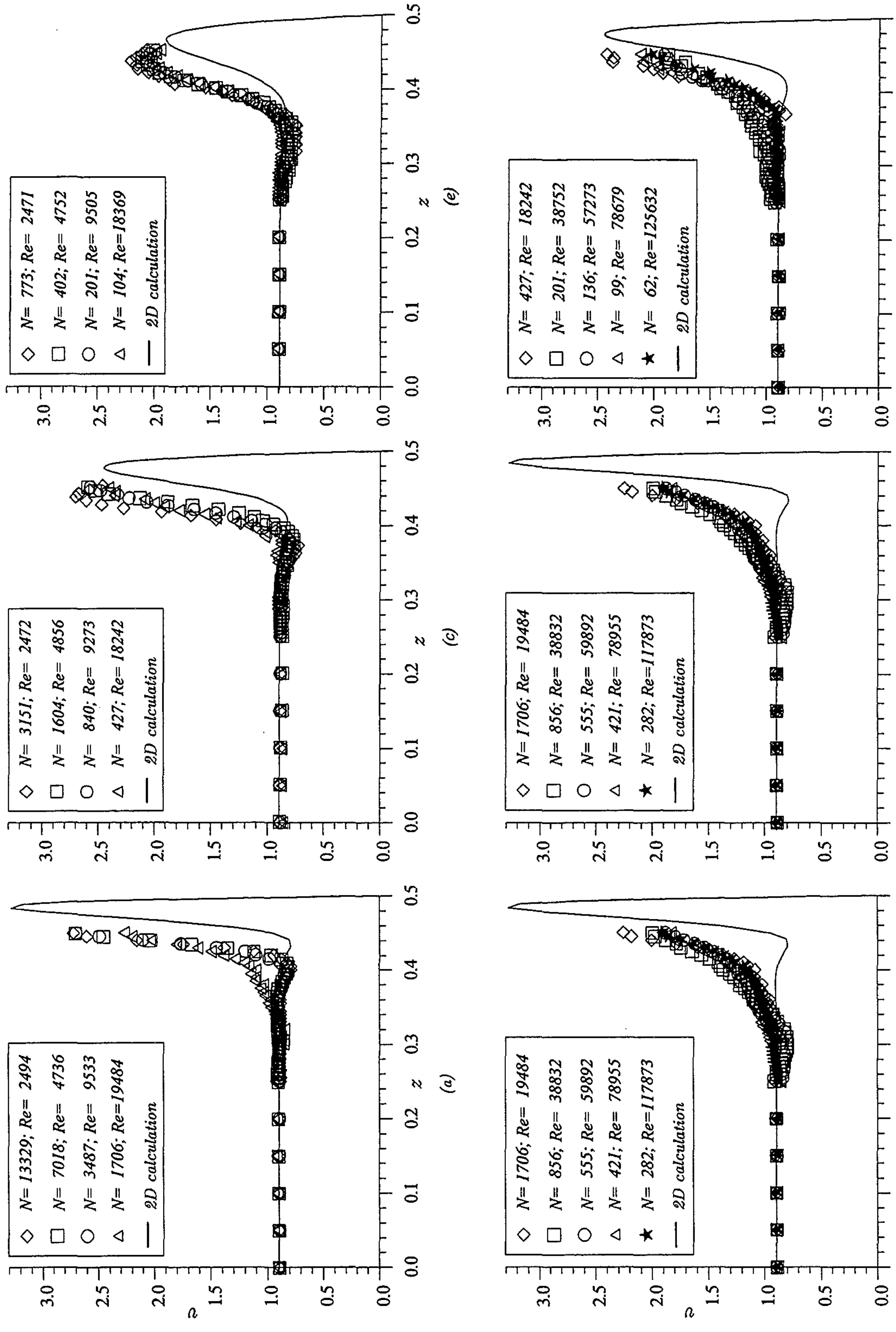

Figure 4-14 Velocity v as a function of z for different N and M. (a), (b) $M = 4993$.
(c), (d) $M = 2417$.
(e), (f) $M = 1197$.

4.2.2 Temperature distribution within the liquid

The heat transfer relations known from OHD contain usually a pressure drop correlation, which takes into account the momentum transport. In OHD the pressure drop correlation indicates the degree of turbulence (Blasius or Prandtl type) and thus describes integrally the turbulence structure. Here, we also investigate a forced convection flow. Therefore, also the temperature distribution within the fluid depends mainly on the velocity and turbulence structure within the liquid.

In order to outline the different heat transfer behaviors of MHD and OHD flows we first discuss the laminar heat transfer. The laminar heat transfer is based on pure heat conduction in $z-$direction.

Laminar OHD flows are characterized by a parabolic velocity profile (Poiseuille-flow), where the highest velocity appears in the ducts center and the flow velocity decays monotonically towards the wall. In MHD flows in ducts with thin electrically conducting walls, however, the highest flow velocity is located near the side walls, see e.g. figures 1-1b, c in §1. Now, if the side wall is heated the heat flux removed from the wall is determined by the flow rate adjacent to the heated wall. The flow rate near the side wall in the MHD flow is higher than in the laminar OHD flow at the same Reynolds number Re, because in the MHD flow a high side wall velocity jet exists. Consequently, heat flux removable in a laminar MHD flow is higher than in the same OHD flow. This is expressed by a lower dimensionless fluid-wall interface temperature Θ.
In figure 4-15 the calculated temperature Θ of an OHD flow (—) and a MHD flow (— —) at a Reynolds number $Re = 2.34 \cdot 10^3$ are plotted as a function of z. Since the flow rate of the MHD flow adjacent to the heated wall is higher compared to OHD the dimensionless temperatures at $z = 0.5$ are lower, which supports the previous consideration. Due to the lower core velocity of the MHD flow the temperature gradient across the duct in z-direction is higher as in OHD, which is also confirmed by the figure 4-15.

In the experiment for the OHD flow at low Re the temperature distribution revealed a different result, see symbols $\diamondsuit$ in figure 4-15. The explanation for this behavior is quite simple. At the Reynolds number investigated in the OHD flow buoyant effects play a significant role. If one calculates the relevant Grashof number Gr ($Gr = (\Delta\rho g d^3)/(\rho\nu^2)$) a value of $3.05 \cdot 10^8$ is obtained, which is already in the unsteady turbulent buoyant convection regime. The influence of buoyancy in the OHD flow is clearly expressed in the figure 4-15 by the smooth temperature distribution.
For higher Hartmann numbers ($M \geq 10^2$) buoyant effects are suppressed by electromagnetic damping. Thus, buoyant effects play no longer a significant role in the experiment. (The reason for the strong electromagnetic damping of convectional motion in this case is that the gravity vector and the magnetic field vector are parallel.) The convection pattern which would evolve due to the applied heat flux would lead to a vortex motion in which the vortex axis is perpendicular to the magnetic field. However, such a vortex is damped at most by the Hartmann breaking. As a result these vortices are suppressed by the mechanisms explained in §1.

At Hartmann numbers $M > 0$ and the same Reynolds number $Re = 2.34 \cdot 10^3$ as in the OHD case the measured and the calculated temperature distributions agree at least

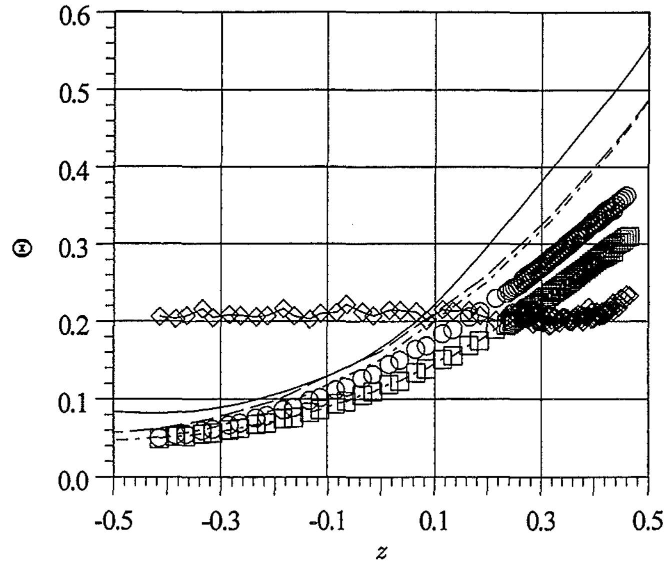

Figure 4-15 Temperature Θ as a function of z in the plane $y = 0$ at $x = 12$ for different M in a laminar flow with $Re = 2.34 \cdot 10^3$. The lines indicate the calculated values, whereas the symbols denote the experimental values. (—, ◇) $M = 0$ OHD; (— —, ○) $M = 1197$; (· · ··, □) $M = 4993$.

qualitatively. The measured temperatures show in the side wall region approximately 20% lower values than the calculations.

Finally, as the Hartmann number increases, the heat transfer also increases which is expressed by lower fluid-wall interface temperatures. The reason for this is that with increasing Hartmann number M the velocity jet becomes larger and, additionally, the jet moves nearer to the heated wall. This result is both confirmed by the experiment as well as by the calculation as demonstrated by figure 4-15.

In the following sequence of figures 4-16a–g, the Reynolds number at a fixed Hartmann number of $M = 4993$ is gradually increased. Simultaneously the turbulence intensity is recorded.

For the highest investigated Hartmann number $M = 4993$ the flow remains laminar up to Reynolds numbers of $Re = 7.8 \cdot 10^3$. Consequently, the temperature distribution measured in the plane $y = 0$ agrees rather well with the values calculated using the laminar model.

A further increase of the Reynolds number leads to first instabilities appearing at the position where the highest velocity gradients exist, see grey marked circle in figure 4-16c. The core flow, however, remains laminar. The appearance of a turbulent flow motion within the thermal boundary layer enhances the spanwise heat transfer. But, the turbulence intensities found for $Re < 1.5 \cdot 10^4$ are quite small (in the range of 5%) and, therefore, do not lead to a significant enhancement of the heat exchange between core and side layer. Therefore, the measured temperature distribution agrees quite well with the calculated one.

If the Reynolds number is increased gradually to values of $Re > 1.5 \cdot 10^4$, the turbulence intensity increases. Additionally, a second peak of the turbulence intensity

near the other inflection point of the velocity profile appears. This peak is located at the position where the side layer matches the core (see circle in figure 4-16d). The high turbulence intensities, which exist within the thermal boundary, lead to a significantly increased transverse heat exchange between the side layer jet and the laminar core flow. This enhanced heat transfer originating from the turbulent flow motion is expressed by higher fluid temperatures in the core flow than calculated with the laminar model. Correspondingly, the increased heat transfer leads to lower fluid temperatures in the side layers and at the fluid wall interface at $z = 0.5$ than predicted by the laminar model.
For Reynolds numbers $Re > 3 \cdot 10^4$ the transverse turbulent heat transfer leads even to a plateau of the temperature as the experimental results show in the figures 4-16e, f. The effectivity of the turbulent flow motion with respect to the heat transfer is expressed by the fluid temperature near the wall which is about 50% lower than the value calculated using the laminar model. This means that the turbulent flow motion in the wall adjacent region leads to a heat transfer enhancement by a factor of 2.

If the Reynolds number is further increased to values of $Re > 10^5$, the turbulence intensity also grows. Additionally, the region of turbulent flow motion increases. Correspondingly, the laminar core flow domain gradually shrinks. But, the measured temperature distribution does not reveal an enhancement of the heat transfer. Moreover, as figure 4-16g shows, the measured values of the dimensionless temperatures nearly coincide with the data calculated for a laminar heat transfer. The reason for this behavior is that with increasing velocity the thermal boundary layer decreases. At the $x-$position and at the Reynolds number $Re = 1.2 \cdot 10^5$ the thermal boundary layer is approximately of the size of the laminar sublayer of the side wall jet near the wall. In this laminar sublayer the heat transfer is governed by pure heat conduction and even if the turbulence intensity in the side layer is quite high it does not contribute to this heat transfer process.

In the figures 4-17-4-19 the same variation of the flow velocity is performed for other levels of the Hartmann numbers investigated, namely $M = 2417$, $M = 1197$, and $M = 0$ (OHD flow).
In case of $M > 0$ and non-laminar flow the turbulence level at the same Reynolds decreases as M decreases, because the velocity gradients of the side layer jet get smaller. As a result the transverse heat transfer for low Hartmann numbers is weaker than for higher Hartmann numbers. The decrease of the heat transfer with descending M is expressed by higher fluid-wall interface temperatures. In the experiment the same behavior is found as a comparison of the graphs 4-16f, 4-17f, 4-18f and 4-19f demonstrates.
Nevertheless, the measured temperatures of the turbulent MHD flows near the wall are still lower than the values calculated using a laminar MHD flow model. The computational results of the laminar MHD temperature distribution are embedded in all figures in form of a line.

In order to compare the heat transfer of a turbulent OHD duct flow with a turbulent MHD flow the measured and calculated temperature distribution in a turbulent OHD flow are shown in figure 4-19. As mentioned in §2 the temperature distribution has been calculated with the $k - \varepsilon-$model.

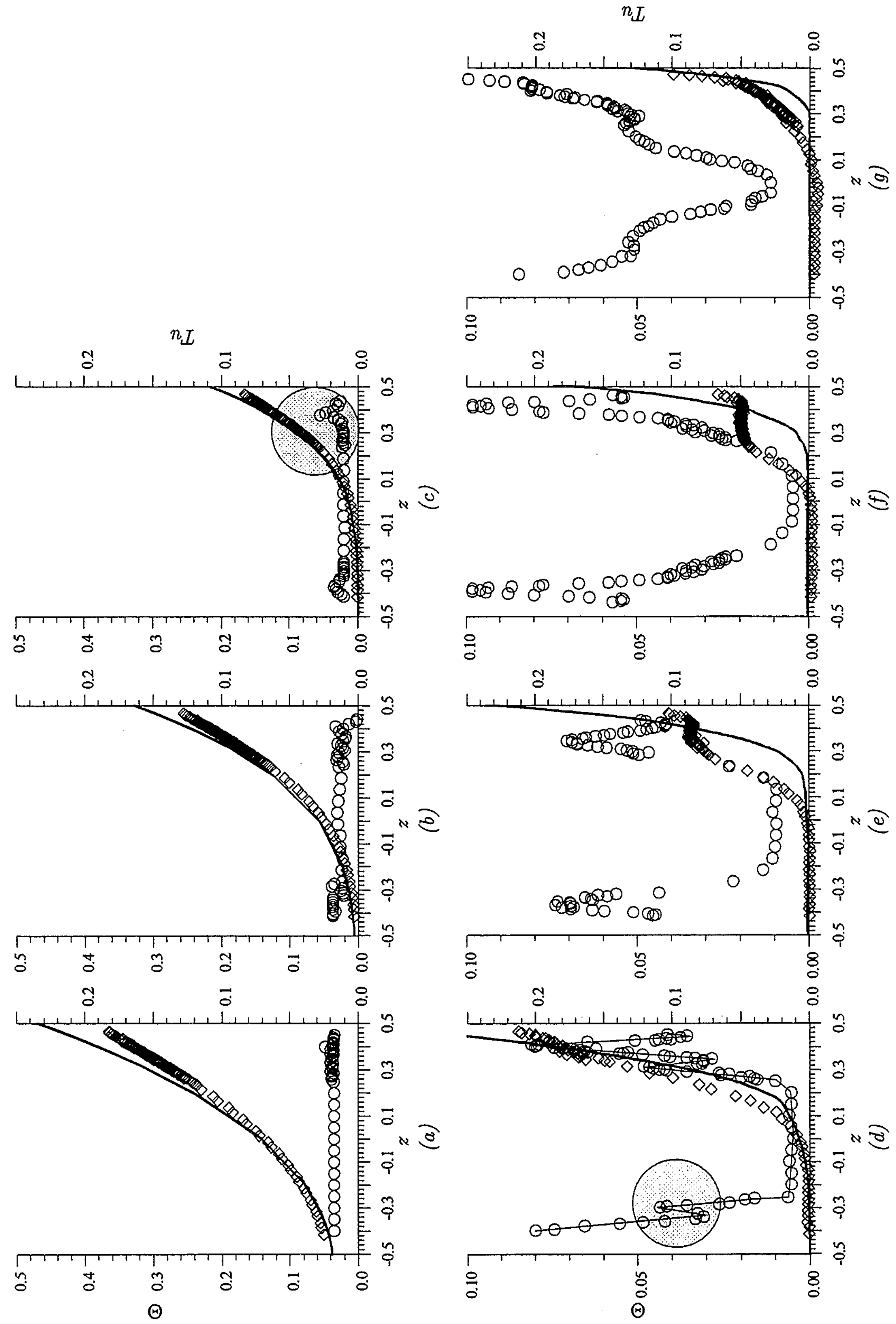

Figure 4-16 Temperatures Θ (◇) and turbulence intensity Tu (○) as a function of z in the plane $y = 0$ for different Re (N) at $M = 4993$. The lines indicate the calculated temperature values for a laminar flow. (a) $Re = 2493$ ($N = 13329$); (b) $Re = 4736$ ($N = 7018$); (c) $Re = 9533$ ($N = 3487$); (d) $Re = 19484$ ($N = 1706$); (e) $Re = 38787$ ($N = 857$); (f) $Re = 59892$ ($N = 555$); (g) $Re = 117873$ ($N = 282$).

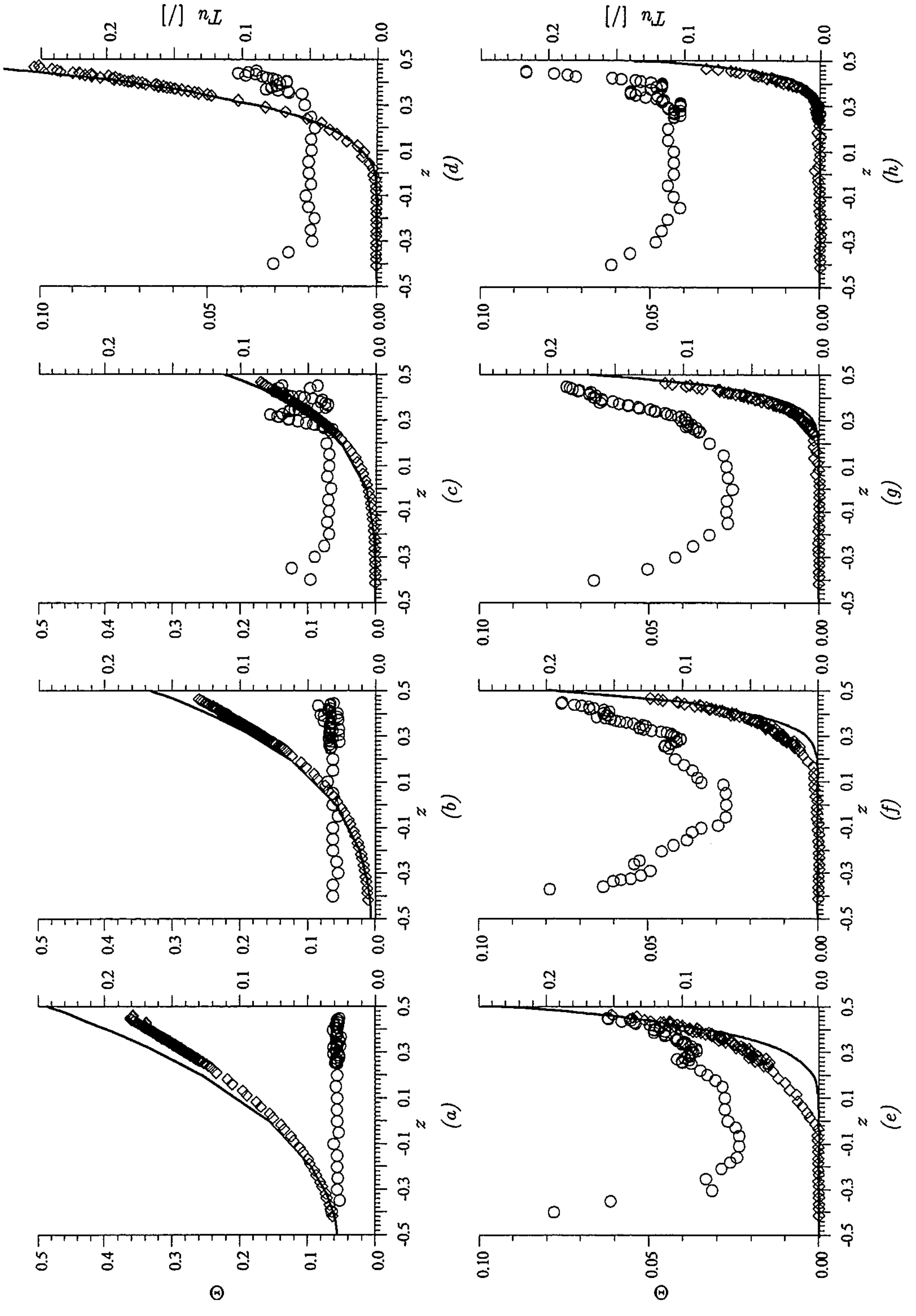

Figure 4-17 Temperatures Θ (◇) and turbulence intensity Tu (○) as a function of z in the plane $y = 0$ for different Re (N) at $M = 2417$. The lines indicate the calculated temperature values for a laminar flow. (a) $Re = 2472$ ($N = 3151$); (b) $Re = 4856$ ($N = 1604$); (c) $Re = 9273$ ($N = 840$); (d) $Re = 18242$ ($N = 427$); (e) $Re = 38752$ ($N = 201$); (f) $Re = 54092$ ($N = 144$); (g) $Re = 78679$ ($N = 99$); (h) $Re = 125632$ ($N = 62$).

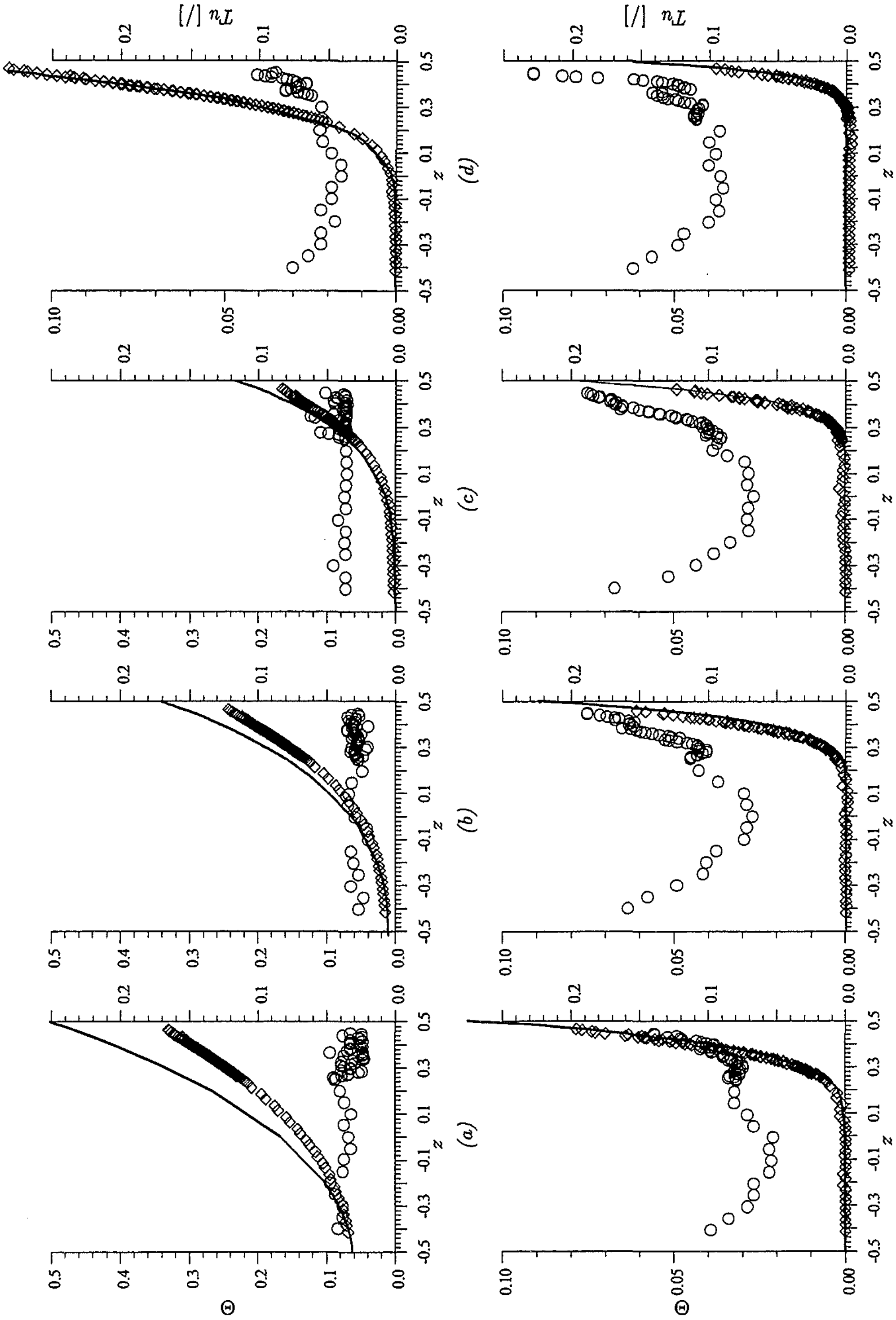

Figure 4-18 Temperatures Θ (◇) and turbulence intensity Tu (○) as a function of z in the plane $y = 0$ for different Re (N) at $M = 1197$. The lines indicate the calculated temperature values for a laminar flow. (a) $Re = 2471$ ($N = 773$); (b) $Re = 4752$ ($N = 402$); (c) $Re = 9504$ ($N = 201$); (d) $Re = 18369$ ($N = 104$); (e) $Re = 37459$ ($N = 51$); (f) $Re = 57891$ ($N = 33$); (g) $Re = 76416$ ($N = 25$); (h) $Re = 119401$ ($N = 16$).

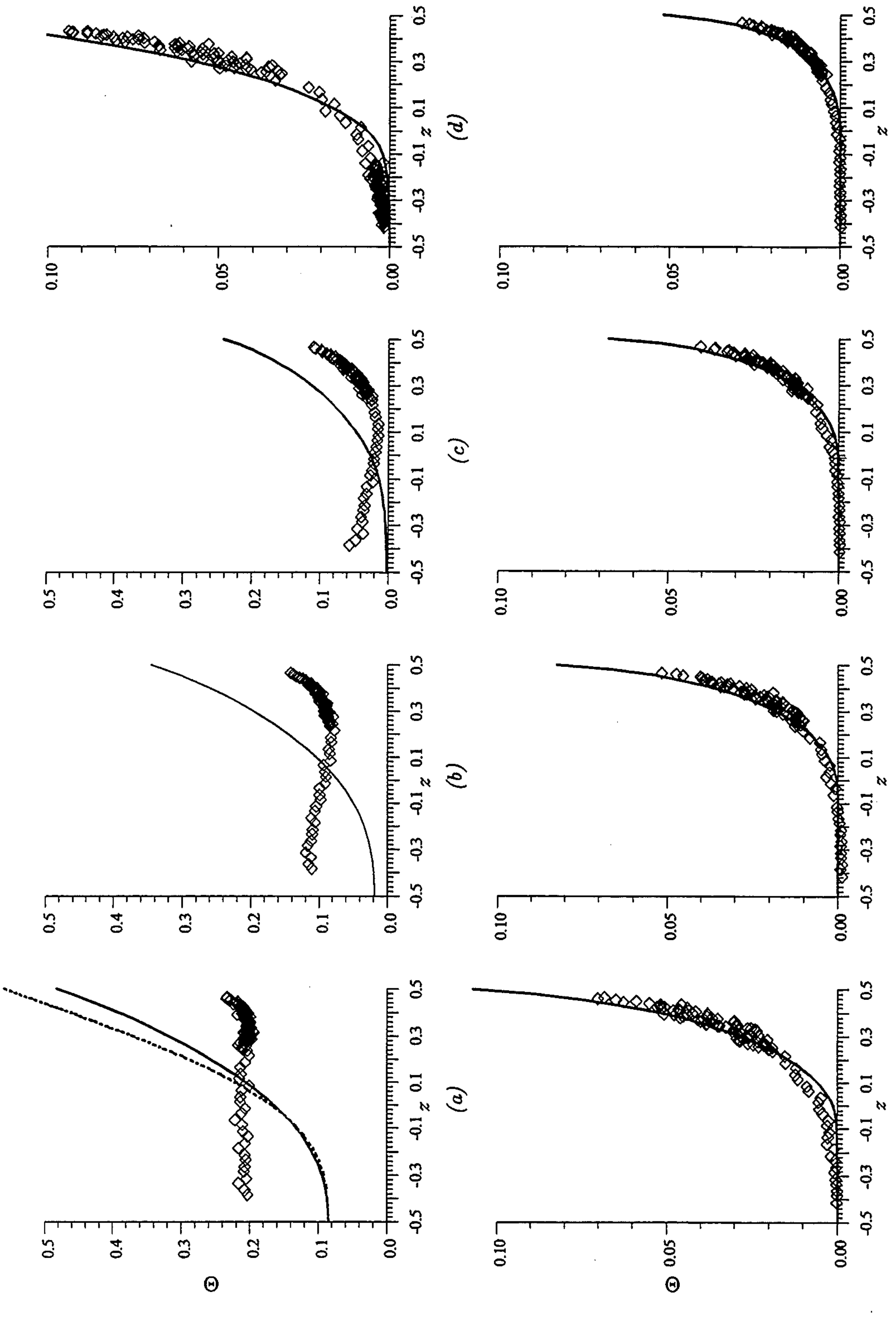

Figure 4-19 Temperatures Θ (◇) as a function of z in the plane $y = 0$ for different Re for an OHD flow ($M = 0$). The lines indicate the calculated temperature values for an OHD flow. (a) $Re = 2673$; (b) $Re = 4763$; (c) $Re = 9173$; (d) $Re = 18046$; (e) $Re = 37481$; (f) $Re = 57956$; (g) $Re = 77190$; (h) $Re = 119600$.

Generally, the heat transfer in turbulent MHD flows is larger than in turbulent OHD flows at the same Reynolds number, which can be explained by the higher flow rate near the side wall region.
The influence of the Hartmann number on the heat transfer can be summarized:

- As M increases, the magnitude of the side layer jet increases and the side layer moves towards the heated wall. This increases the velocity gradient near the walls.
- As M increases the side layers becomes destabilized. This leads to a higher turbulence intensity Tu with increasing M. The turbulence intensity level in MHD flows at the same Reynolds number ($Re > 3 \cdot 10^4$) near the heated wall is higher than in corresponding OHD flows.
- The turbulent structures in MHD flows are large scale structures, which act in transverse direction over larger distances than the turbulence structures being present in OHD flows.

4.2.3 The wall temperatures

The temperatures at the fluid-wall interface serve from an engineering point of view the most interesting results since the results obtained there determine the achievable heat flux removable from the wall. As described §1most heat transfer problems are thermally developing. Unfortunately, for such developing flows of fluids with low Prandtl numbers no heat transfer correlations are given in engineering textbooks. In technical systems usually the correlations for thermally fully developed flows are used as a conservative assessment, because the Nusselt numbers in developing flows are higher than in already developed flows. The Nusselt number Nu is the inverse of the dimensionless interface temperature Θ, i.e. $Nu = 1/(T_{Wall} - \overline{T_{bulk}})$.
In figures 4-20a-f the dimensionless fluid-wall interface temperatures $\Theta_{m3,i}$ of an OHD flow in the plane $y = 0$ are plotted as a function of x for several Reynolds numbers Re.
Both, the calculated and the experimental results reveal that the upstream heat flux in the structural material for each Reynolds number leads to a temperature at $x = 0$ different from zero. This effect decreases as Re increases because the heat removal from the wall grows with higher velocities. The reason for the upstream heating of the fluid is that the heat conductivities of the fluid and the wall and the wall are comparable.

The fluid-wall interface temperatures $\Theta_{m3,i}$ for a laminar OHD flow in the experiment agree qualitatively with the numerically calculated values, see figure 4-20a. Quantitatively, however, deviations of about 25% are found. As previously discussed these deviations originate from buoyancy effects present at low Re.
As Re increases, the fluid-wall interface temperatures decrease both due to the higher average flow velocity and due to the turbulent transport of heat towards the core of the flow. Nevertheless, the interface temperatures calculated with the $k - \varepsilon$ −model and the standard constants agree rather well with the measured values throughout the whole Reynolds number range investigated.

How is the interface temperature changed if MHD is involved?
Let us first discuss the temperature distribution of the laminar flow. In figure 4-21a the dimensionless temperature at the fluid-wall interface along the $x-$axis is shown for the Reynolds number of $Re = 2276$ and different Hartmann numbers.
A comparison of the calculated values for a laminar OHD (−·−) flow with the laminar MHD flows for $M = 1197$ (− −) and $M = 4993$ (−) and the same heat flux shows that in MHD flows the heat transfer is enhanced.
Comparing the both MHD flows leads to the result that with increasing Hartmann numbers the heat removal from the hot wall also increases. Generally, MHD flows in the configuration investigated show lower wall temperatures than OHD flows because the formation of high velocity side layer jets in MHD flows enhance the flow rate near the hot wall.
The experimental results shown in the figure 4-21a partially confirm the explanation for small $x-$ values. However, at a larger axial distance, i.e.e if $x > 6$, a critical temperature difference is exceeded, which causes in addition to the forced convection a buoyant flow. This superposition leads for $x > 6$ to an increased heat transfer in the OHD flow.

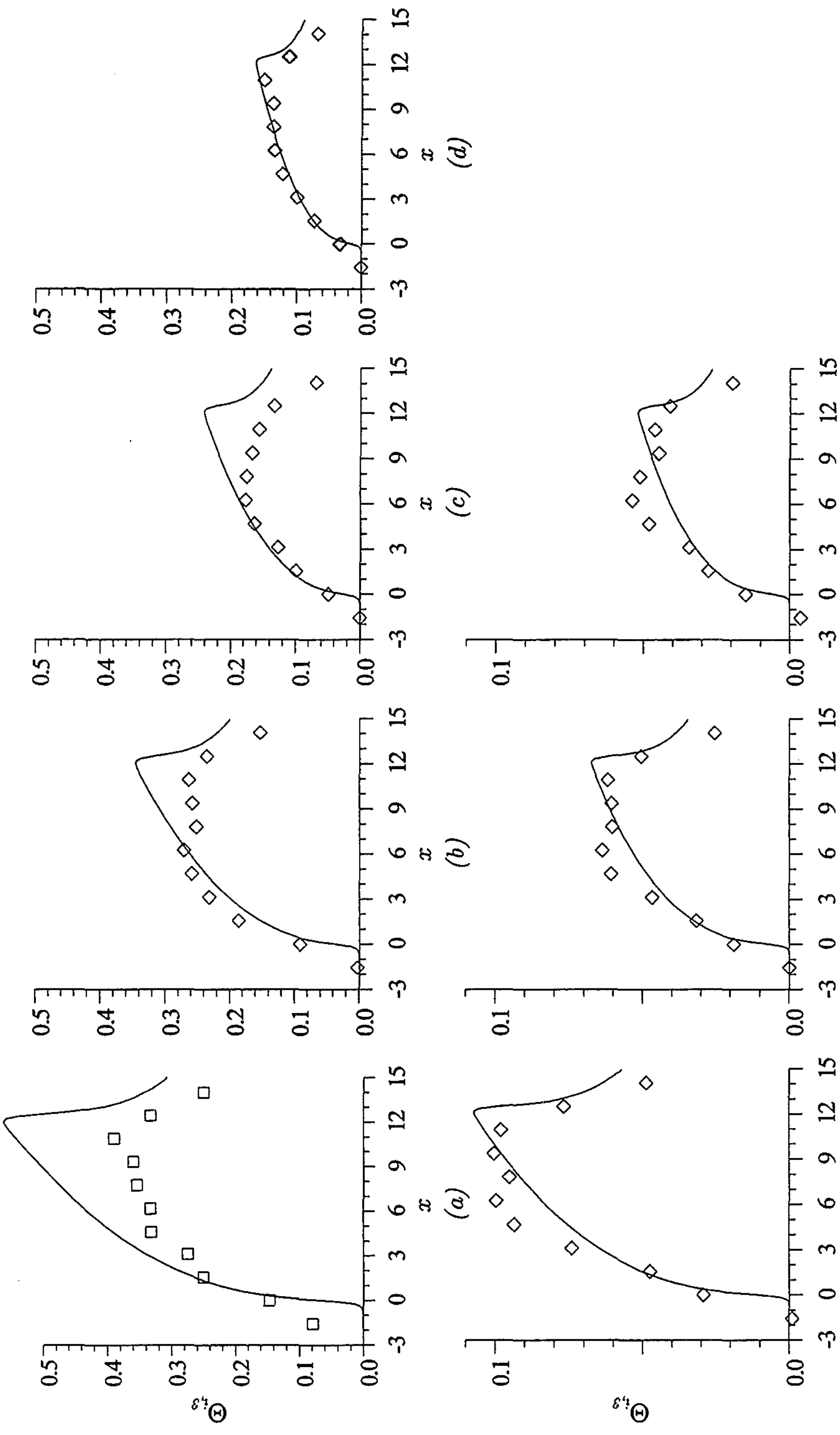

Figure 4-20 Fluid-wall interface temperature $\Theta_{m3,i}$ in the plane $y = 0$ as a function of x for a hydrodynamic turbulent flow. The lines (—) indicate the values calculated with the $k - \varepsilon -$ model. (a) $Re = 2273$, ($Pe = 59$); (b) $Re = 4763$, ($Pe = 121$); (c) $Re = 9173$, ($Pe = 240$); (d) $Re = 18046$, ($Pe = 488$); (e) $Re = 37481$, ($Pe = 962$); (f) $Re = 77719$, ($Pe = 1913$); (g) $Re = 119060$, ($Pe = 2816$).

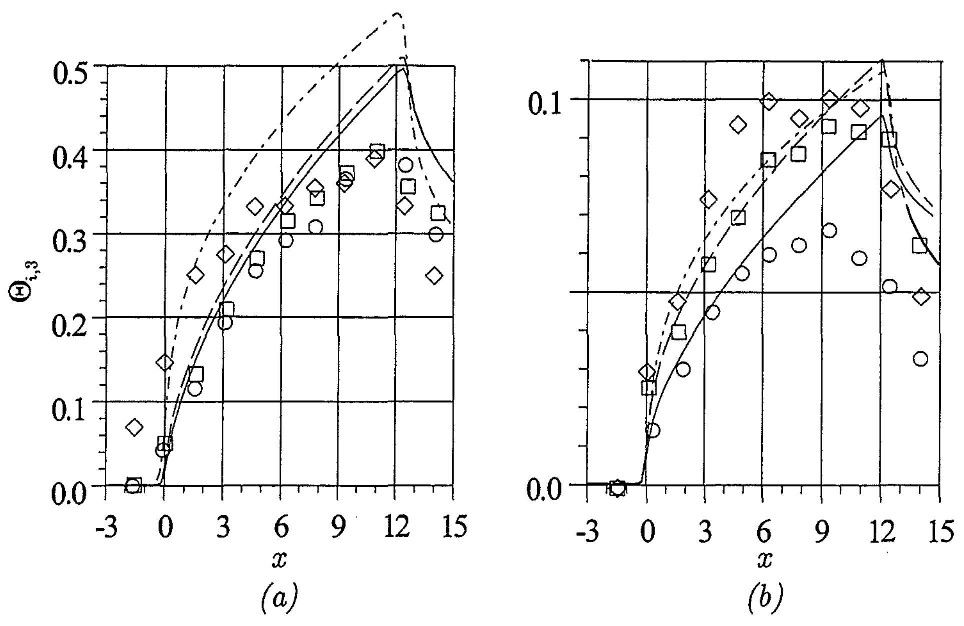

Figure 4-21 Fluid-wall interface temperature $\Theta_{m3,i}$ in the plane $y = 0$ as a function of x for different Re. The lines indicate the calculated values for OHD flow (— · —), $M = 1197$ (— —) and $M = 4993$ (—). The experimental data are displayed by symbols OHD (◇), $M = 1197$ (□) and $M = 4993$ (○) . (a) $Re = 2276$. (b) $Re = 3.7 \cdot 10^4$.

In the case of turbulent flows the situation is in principle the same as figure 4-21b shows. The curve (—·—) shows the calculated wall temperature along x for a turbulent OHD-flow at a Reynolds number of $Re = 3.7 \cdot 10^4$. The other two curves present the results of the temperature distribution obtained for a laminar MHD-profile at the same Reynolds number. The computational results demonstrate that even if the MHD flow at such high Reynolds numbers would be laminar the heat transfer is increased compared to a turbulent OHD flow.

At the Reynolds number $Re = 3.7 \cdot 10^4$, however, the MHD flow is also turbulent. The experimental results, which are marked by symbols in the figure 4-21b, show that MHD turbulence enhances the heat removal from the hot wall. The dimensionless wall temperatures measured are for all Hartmann numbers significantly lower than the results of the laminar calculations. With increasing Hartmann number the deviations between the laminar calculation and the experimental values increase. Thus, an increasing M leads to a technically usable heat transfer enhancement. If we compare the experimental results of MHD flow ($M = 4993$) with the OHD flow shown in figure 4-21b the MHD flow shows a Nusselt number being nearly twice as high as the OHD flow.

In the figures 4-23 to 4-25 the fluid-wall interface temperatures $\Theta_{m3,i}$ along x are shown for increasing Reynolds numbers at three different Hartmann numbers. In each subgraph the symbols indicate the experimentally obtained data, whereas the full lines present the calculated data using a laminar MHD flow at the same Reynolds number as an input. The dotted lines also drawn in each graph show the temperature distribution which would be obtained for a slug flow type velocity profile. The temperature distribution for a slug flow velocity profile is shown, because this model has been widely used in the past for fusion blanket designers due to the lack of experimental results.

The fluid-wall interface temperature distributions calculated a slug flow velocity profile shows at all Hartmann numbers and Reynolds numbers investigated higher wall temperatures than the calculations with the correct MHD velocity profile. Moreover, the temperatures obtained with the slug flow velocity assumption are by far higher than the experimental data. Therefore, the slug flow assumption represents in any case a may be too conservative assessment for liquid metal cooled fusion blanket designs.

In case of laminar MHD flows ($Re \leq 9 \cdot 10^3$) a good agreement between numerically calculated and experimentally obtained data is found. As the figures a-c in the graphs 4-23-4-25 shows both the temperature rise and the temperature decay are quite well predicted. A quite more surprising result of the figures 4-23-4-25 is that in the Reynolds number range $9 \cdot 10^3 \leq Re \leq 1.8 \cdot 10^4$ and $Re \geq 8 \cdot 10^4$ the experimental and the theoretical results also agree quite well, although the MHD flow is far of being laminar. The reason in both cases is the behavior of the dynamical (viscous) and thermal boundary layers. In the low turbulent Reynolds number range the turbulence intensities which are responsible for the transverse transfer of heat are quite low. Therefore their contribution to the heat transfer is quite small. Due to this no remarkable differences between the turbulent and the laminar case appear. This effect gets more and more pronounced as the Hartmann number decreases because the velocity gradients get smaller and consequently the turbulence level falls.

At high flow velocities (large $Re > 10^5$) the thermal boundary layer at the end of the heated length ($x = 12.5$) has not penetrated into the region of high turbulence intensity. It is still within the laminar subregion of the viscous side layer jet. There, however, the heat transfer is governed by laminar heat conduction. Consequently, the heat transfer is not enhanced by the turbulent flow motion.

As the Hartmann number decreases the side layer width increases. Therefore, the length in $x-$direction at which a significant enhancement by turbulent flow motion can be expected, also increases.

From figure 4-22 a measure of the quality of the heat transfer can be taken.

In the case of laminar conductive heat transfer in the MHD flow the temperature distribution along x can be expressed by a self-similar solution scaled with x/Pe. This means that at a constant Hartmann number (fixed laminar velocity profile) and a given Pe the temperature at the fluid-wall interface is uniquely given at each $x-$position. For a Hartmann number of $M = 4997$ and laminar heat transfer the calculated values are shown in figure 4-22. As one can see from this figure the laminar heat transfer splits off in three regions.

- *Region I* for $x/Pe \leq 3 \cdot 10^{-3}$ where the fluid-wall interface temperature in the calculation obeys the relation $\Theta_{m3,i} \sim (x/Pe)^{0.63}$. Here, the thermal boundary layer has not penetrated into the region where turbulent flow motion appears. Therefore, the heat transfer is based on laminar heat transport. The experiment shows in this range an good agreement with the calculation. A fit through the experimental data yields the following proportionality:

$$\Theta_{m3,i} \sim (x/Pe)^{0.57}. \tag{4.13}$$

- In the intermittent *region II* turbulent heat transport measured in the experiments leads to an enhanced heat transfer compared to laminar flows as the figure 4-22 shows. A fitting procedure for the experimental data based on the last minimum squares leads to the relation:

$$\Theta_{m3,i} \sim (x/Pe)^{0.4}. \tag{4.14}$$

- Finally, in *region III* at low Reynolds numbers (high Pe) the heat transfer is based on conduction (laminar heat transfer). The calculation leads there to the following proportionality $\Theta_{m3,i} \sim (x/Pe)^{0.33}$. The fit through the experimental data shows a nearly perfect agreement in the exponent. The fit result is:

$$\Theta_{m3,i} \sim (x/Pe)^{0.35}. \tag{4.15}$$

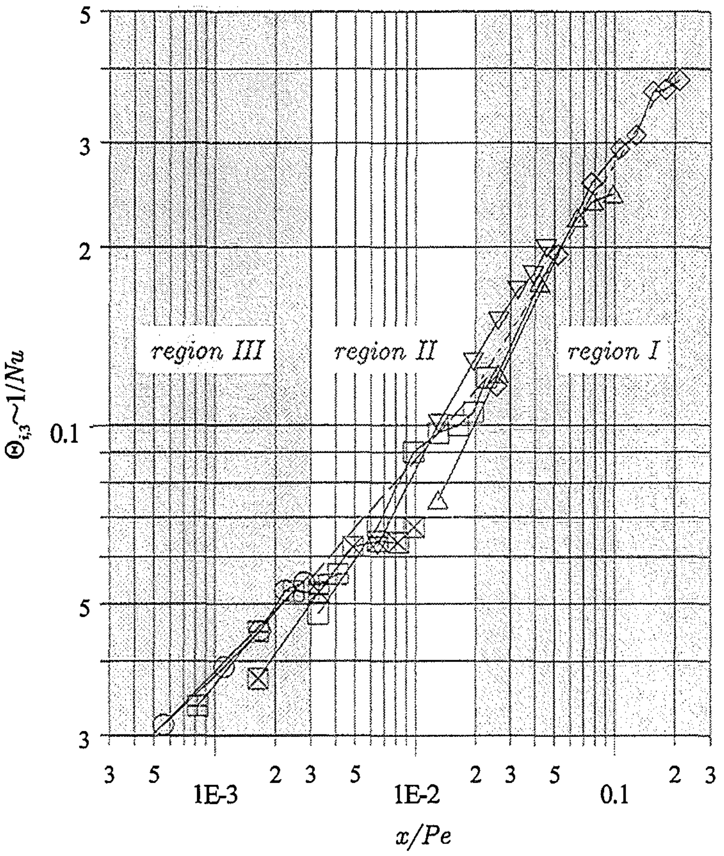

Figure 4-22 Fluid-wall interface temperature $\Theta_{m3,i}$ in the plane $y = 0$ as a function of x/Pe for a MHD flow in a rectangular duct with thin electrically conducting walls at $M = 4993$. The lines indicate the values calculated for the heat transfer in a laminar MHD flow . (◇) $Re = 2493$; (△) $Re = 4736$; (▽) $Re = 9532$; (□) $Re = 19461$; (⊠) $Re = 38832$; (⊞) $Re = 59357$; (○) $Re = 117872$.

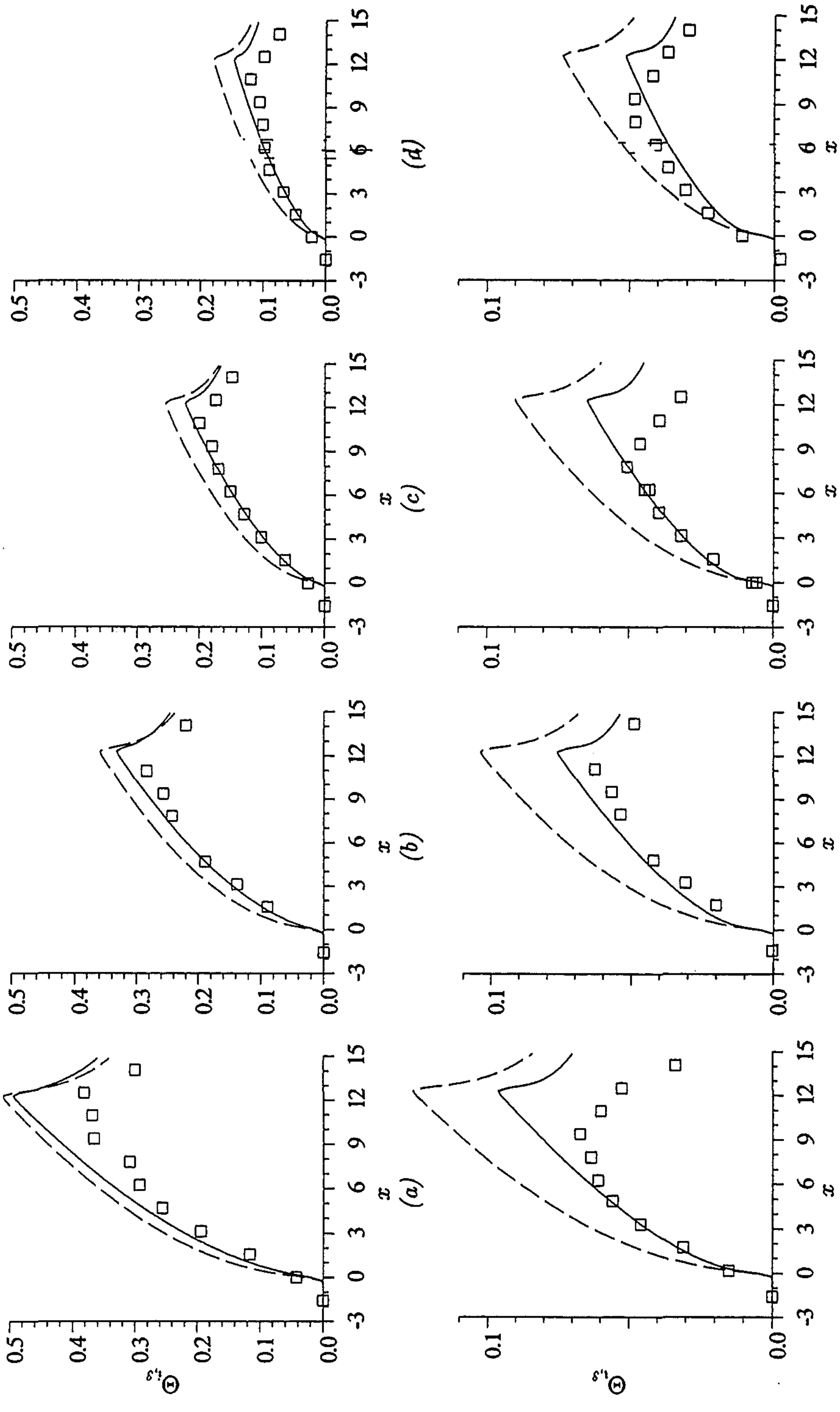

Figure 4-23 Fluid-wall interface temperature $\Theta_{m3,i}$ in the plane $y = 0$ as a function of x at $M = 4993$. The lines (–) indicate the values calculated for a laminar flow; (– –) calculation for a slug flow type velocity profile. (a) $Re = 2493$, $(N = 13329)$; (b) $Re = 4736$, $(N = 7018)$; (c) $Re = 9532$, $(N = 3487)$; (d) $Re = 19461$, $(N = 1708)$; (e) $Re = 38832$, $(N = 856)$; (f) $Re = 59357$, $(N = 560)$; (g) $Re = 78768$, $(N = 422)$; (h) $Re = 117872$, $(N = 282)$.

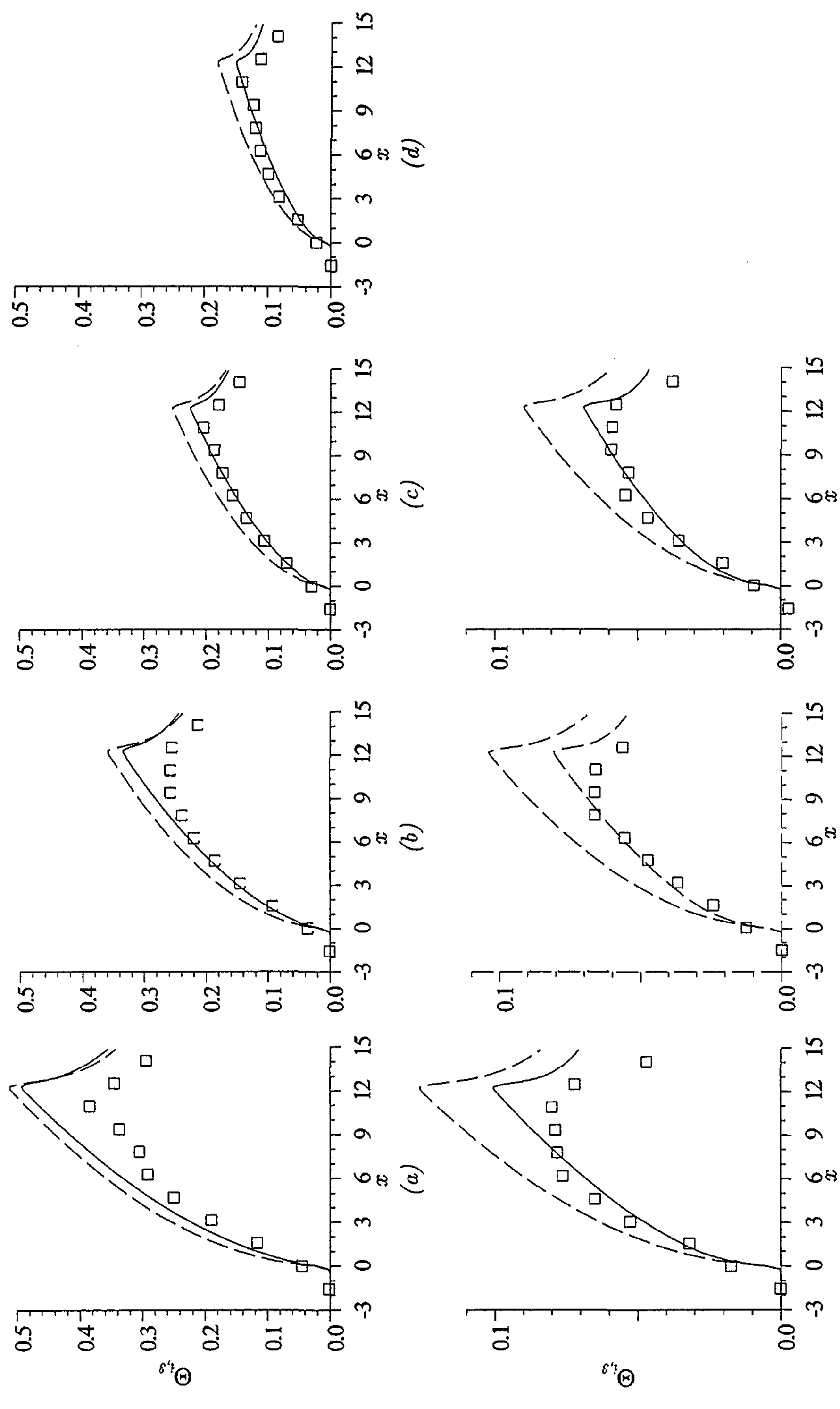

Figure 4-24 Fluid-wall interface temperature $\Theta_{m3,i}$ in the plane $y = 0$ as a function of x at $M = 2417$. The lines (–) indicate the values calculated for a laminar flow; (– –) calculation for a slug flow type velocity profile. (a) $Re = 2472$ ($N = 3151$); (b) $Re = 4856$ ($N = 1604$); (c) $Re = 9273$ ($N = 840$); (d) $Re = 18242$ ($N = 427$); (e) $Re = 38752$ ($N = 201$); (f) $Re = 54092$ ($N = 144$); (g) $Re = 78679$ ($N = 99$).

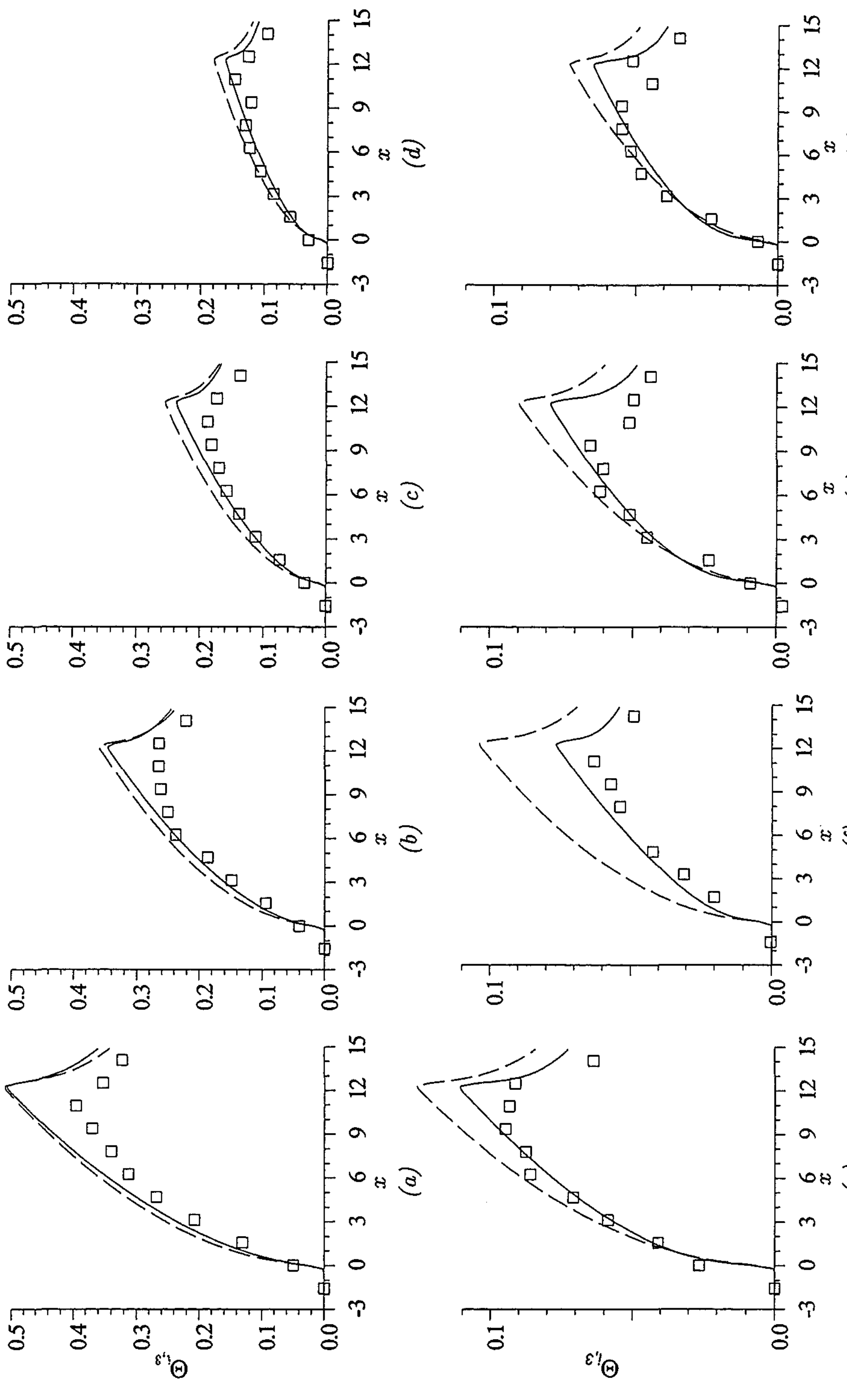

Figure 4-25 Fluid-wall interface temperature $\Theta_{m3,i}$ in the plane $y = 0$ as a function of x at $M = 1197$. The lines (–) indicate the values calculated for a laminar flow; (– –) calculation for a slug flow type velocity profile. (a) $Re = 2471$ ($N = 773$); (b) $Re = 4752$ ($N = 402$); (c) $Re = 9504$ ($N = 201$); (d) $Re = 18369$ ($N = 104$); (e) $Re = 37459$ ($N = 51$); (f) $Re = 57891$ ($N = 33$); (g) $Re = 76416$ ($N = 25$); (h) $Re = 119401$ ($N = 16$).

Chapter 5

Impact on self-cooled blankets

The aim of this chapter is to assess the thermohydraulic performance of the self-cooled liquid metal blanket using the experimental results obtained in the present experiment. The most critical channel is the first wall channel, since it has the highest temperature rise, is facing the highest heat flux and experiences the strongest volumetric heating.

The actual material properties limit the allowable temperature of the first wall to about 550°C in case of ferritic steel and to 750°C for vanadium alloys. The maximum temperature at the wall/liquid metal interface has to be maintained approximately 100°C lower in order to limit corrosion of the structure material by the liquid metal. For an effective electricity production the bulk temperature of the coolant at the blanket outlet should be higher than 400°C. The coordination of these contrasting requirements form the actual design task. The design limitations can be expressed in terms of an upper and lower limit for the coolant channel pressure load to ensure structural integrity and sufficient flow rate for heat removal. The thermohydraulic boundary conditions for a DEMO reactor arising from these conditions are listed in table 5.1.

DEMO specification	*unit*	*Lithium*
magnetic field strength	T	5.00
first wall heat flux	Wcm^{-2}	50.00
flow length along first wall (half outboard)	m	4.00
characteristic first wall duct dimension (a)	m	0.066
max. fluid interface temperature at first wall	$^\circ C$	490
average fluid temperature	$^\circ C$	350
thickness of first wall	mm	8.00
average flow velocity in first wall coolant duct	ms^{-1}	1.50
max. temperature rise at first wall	$^\circ C$	159
pressure drop in first wall using FCI	MPa	1.424

Table 5.1: Thermohydraulic conditions of a self-cooled Lithium blanket for DEMO, see Malang et al. (1995).

The experimental results obtained can be applied to improve self-cooled liquid metal blanket designs with first wall cooling in poloidal direction. The schematics of the flow path as well as the cross-section of a self-cooled liquid metal cooled blanket proposed by Hua and Gohar (1994) or John et al. (1991) is shown in figures 5-1a-c. In order to reduce the amount of coolant systems compared to hybrid concepts like the WCLL (see Giancarli, 1994) or the Dual-Coolant Concept (see Malang et al. 1993), in which two fluids are used, these more advanced blanket concepts take advantage of only one fluid as coolant and breeder. The most preferred option for liquid metals in such concepts is Lithium. Lithium offers a higher Tritium breeding ratio, the ability of a controlled shut down in case of a leak towards the plasma chamber, because Lithium stabilizes the plasma. Although, due to the high solubility of Tritium within Lithium increases the Tritium inventory of a reactor, this high solubility retains Tritium within Lithium in case of LOCA (loss of coolant accident). One of the largest disadvantages of Lithium is the high reactivity of Lithium with other structural materials and with air and water, which demands the development of sophisticated materials.

Due to the arrangement of the blanket in the reactor most of liquid metal flows perpendicular to the magnetic field in poloidal direction. Therefore, these concepts are called poloidal concepts.

In the upper outboard blanket the coolant is fed from the top via a manifold to the rear ducts, flows downward, is turned by 180° in the first wall ducts. There, it flows poloidally upwards. The downflow in the rear channels can be kept low due to the low volumetric heating in this region. The velocity in the first wall channels has to be much higher in order to avoid an unacceptable temperature rise at the fluid wall-interface along the flow path.

To take advantage of the turbulence generation by side wall jets as shown in §4.2 the first wall has to be flat and oriented parallel to the magnetic field.

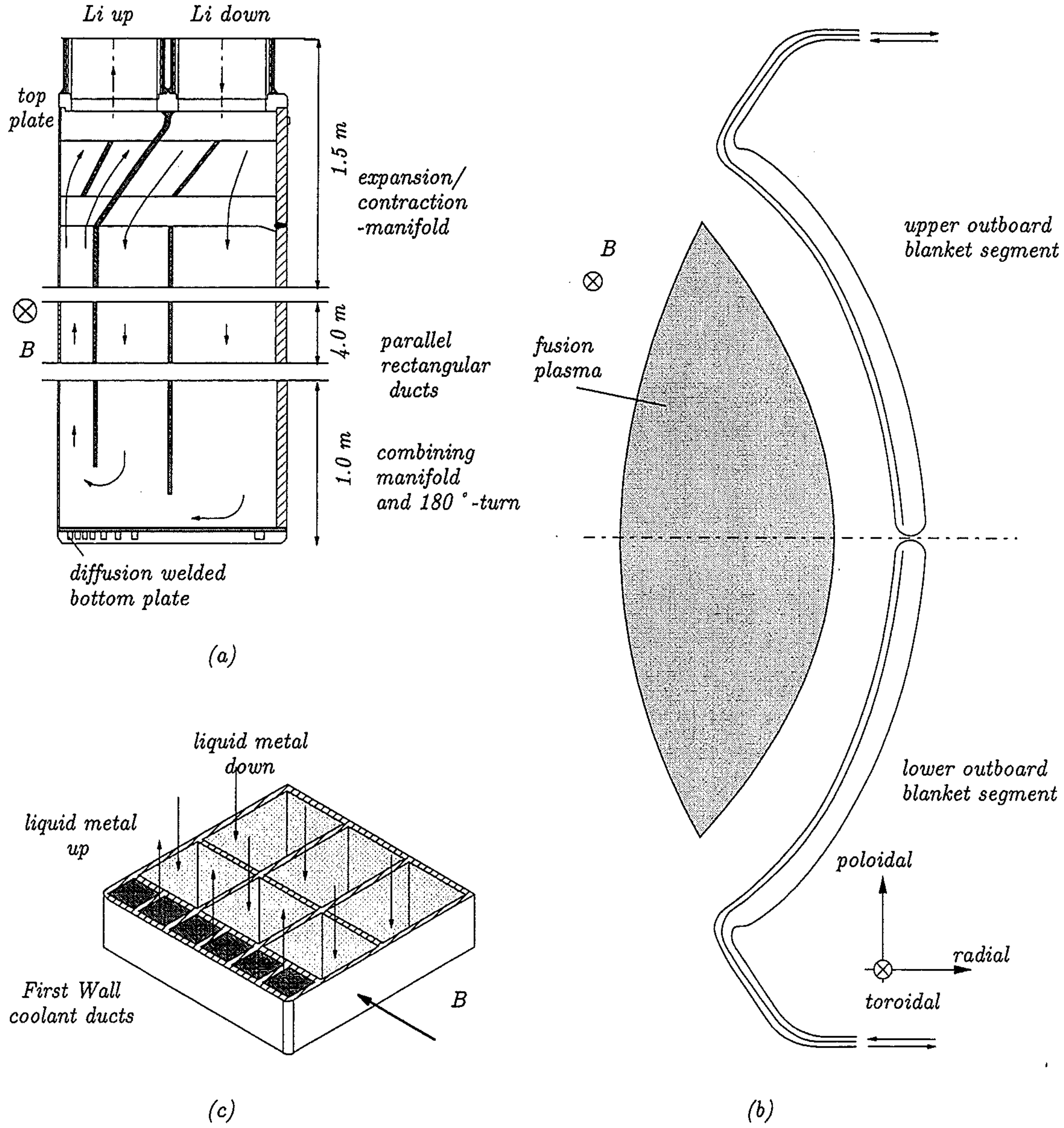

Figure 5-1 (a) Schematics of the liquid metal flow path in a self-cooled poloidal blanket. (b) Arrangment of self-cooled outboard blankets in a TOKAMAK. (c) Cross-sectional cut through a poloidal self-cooled liquid metal blanket.

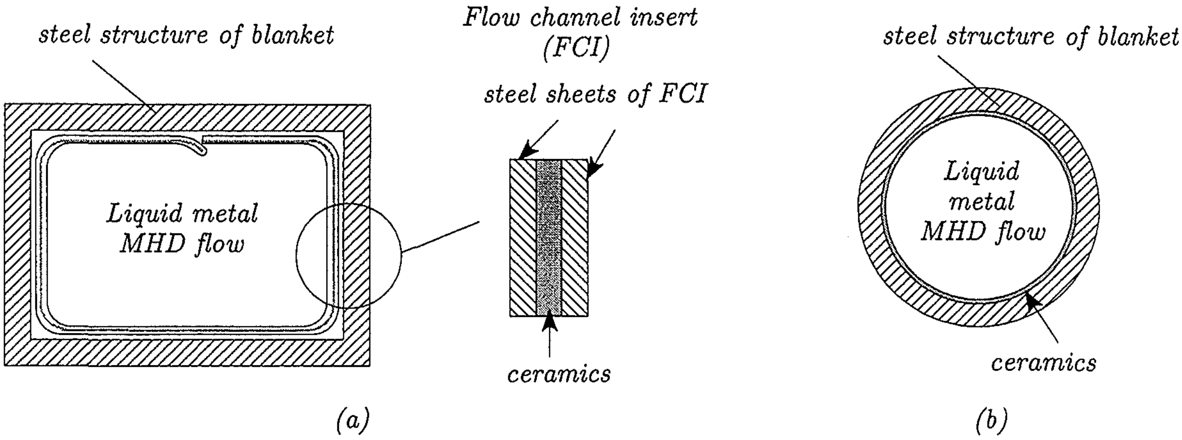

Figure 5-2 (a) Flow channel insert (FCI) fitted loosely in a massive steel strucutre. (b) Direct electrically insulating coating.

Estimates have shown, that self-cooled blankets in Tokamaks with high magnetic field strength (-foreseen are at least 5 Tesla for the DEMO reactor-) and with lithium or lead-lithium as breeder material are hardly or even not feasible without any electrical decoupling of the load carrying walls from the coolant. If the walls in such a blanket concept would consist of only the bare steel structure the MHD pressure drop would exceed the maximum allowable material stress by far. Therefore, two kinds of an electrical insulation are being developed in the fusion program.
One is realized by so-called "Flow Channel Inserts" (FCI). These inserts are fabricated by sandwiching a thin ceramic layer between thin steel sheets (thickness about 0.5mm) which are welded at all edges. The FCI´s are fitted loosely into the ducts. Appropriate slits allow a pressure equalization between the bulk flow and gap flow of the duct wall. A schematics a Flow channel insert is shown in figure 5-2a. It has the advantage that the direct contact between the electrically insulating ceramics and the liquid metal is avoided so that local crack of the ceramics does not lead to a system failure. The drastically lower pressure drop in duct with FCI´s is based on the fact that all electric currents induced in the flow short circuit within the fluid or the thin wall of the FCI. Thus the current density in the fluid is reduced and therefore also the pressure drop. The wall conductance ratio accounting for the pressure drop is that of the thin FCI steel walls.
The viability of FCI´s has already been demonstrated in an experiment at fusion relevant Hartmann numbers by Barleon et al. (1989, 1991). The experimental results showed an excellent agreement with the theoretically predicted values.

The other kind of insulation is based on direct coating the duct surface with insulating ceramic materials which is in contact with the liquid metal. Compared with the FCI technique the pressure drop calculated for a DEMO reactor is drastically smaller (5.9 bars for a direct coating to 40.7 for the FCI technique for the Dual-Coolant Concept, see Malang&Tillack (1995)). However, only small cracks within the insulation layer can change the pressure drastically to higher values, because the currents can short-circuit then within the rather thick walls of the structural material. The requirements for an electrically insulating layer in the ducts of a fusion blanket are:

- compatibility with PbLi or Lithium,
- ability of self-healing of local defects in order to maintain flow characteristics,
- high electric resistance during the whole blanket lifetime at high neutron fluxes.

Due to these large requirements the development of a direct coatings is still an ongoing task.

Studies showed that using lithium as liquid and the FCI technique the MHD pressure drop under DEMO conditions can be kept in tolerable limits if the blankets are divided into two halfs as shown in figure 5-1b. These studies were conducted assuming laminar slug flow not taking into account the improvement of heat transfer by the side wall jet and the hereby induced turbulence.
These effects can reduce the velocity of the liquid metal in the front channel needed to keep the temperature at the first wall interface in the acceptable limit of at maximum $450°C$.

Due to the high neutron flux and the heat flux at the first wall the FCI there covers only the two Hartmann walls and the second wall. In all other parts of the blanket the FCI´s correspond to the technique shown in figure 5-2a. At the first wall the FCI considered is to be open. Because the first wall is 8mm thick the wall conductance ratio at the first wall is $c = 0.048$ for Lithium. All other relevant thermohydraulic data for the MHD heat transfer calculations are given in table 5.2.

Thermohydraulic MHD parameters	*unit*	
wall conductance ratio of Hartmann walls	[/]	0.003
wall conductance ratio of side wall	[/]	0.003
wall conductance ratio of first wall	[/]	0.048
Hartmann number	[/]	28447
Interaction parameter	[/]	7357
Reynolds number	[/]	$1.1 \cdot 10^5$
Prandtl number	[/]	0.047
Peclet number	[/]	5265

Table 5.1: Thermohydraulic boundary conditions for the MHD flow in the first wall duct of a DEMO blanket.

The calculated velocity profile of the MHD flow in first wall coolant duct at DEMO conditions is shown in figure 5-3. Due to the rather thick first wall the side wall jet at the first wall is drastically lower than at the second wall, where the calculation yield about 16 . But, due to the high Hartmann number the velocity gradients at this first

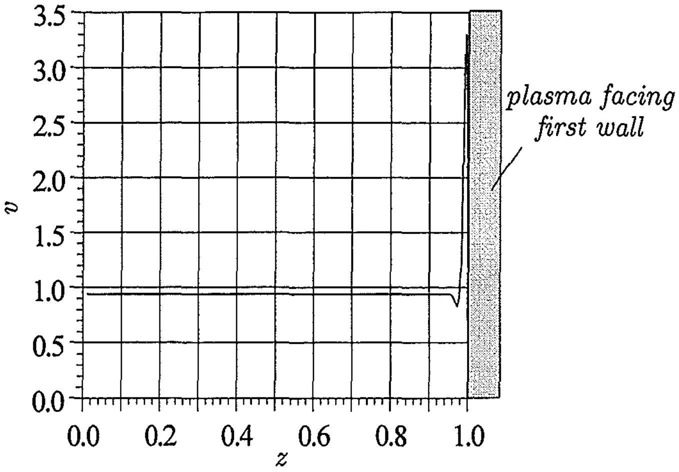

Figure 5-3 Calculated MHD velocity profile in the first wall coolant ducts of a poloidal self-cooled DEMO blanket. $M = 2.84 \cdot 10^4$, $c = 0.003$, $c_{firstwall} = 0.048$.

wall jet are of the same order of magnitude than in the experiment presented here. Thus, as Reynolds number and velocity gradients in the present experiment and in the first wall ducts of a self-cooled Lithium blanket at DEMO conditions are of the same magnitude a turbulent flow motion is more than likely.

If we now extrapolate the experimental results on a self-cooled poloidal Lithium blanket and use instead of the slug flow profile the relevant MHD profile at DEMO conditions, we obtain an heat transfer enhancement of 30%. Or in other terms, we can reduce the flow velocity about 30% (and thus the pressure drop about 30%) in order to get the same temperature rise as in the slug flow model.

If we **additionally** take into account turbulent flow motion we have to split the flow in the regions, where turbulence leads to an enhancement of heat transfer and where not.

For $x/Pe < 3 \cdot 10^{-3}$ (Region I), which corresponds in DEMO to a length of about $1m$ no additional heat transfer enhancement can be expected, since the thermal boundary layer has not reached the turbulent flow domain. For $3 \cdot 10^{-3} \leq x/Pe \leq 2 \cdot 10^{-2}$ (Region II ,according to figure 4-22), which corresponds to a length of $7m$ (!) a heat transfer enhancement of a factor 2 compared to the slug flow assumption is very likely. This length of $7m$ is more than the splitted blanket is long.

Combining both effects from Region I and II a total heat transfer enhancement of 86% compared to slug flow can be assessed.

Or vice versa, maintaining the same temperature rise as in the slug flow design the flow velocity can be reduced and thus, the pressure drop in the first wall coolant ducts can be reduced. Even with the reduced velocity the flow will be turbulent.

Chapter 6

Conclusions

The heat transfer in a magnetohydrodynamic (MHD) flow has been studied in a rectangular duct with thin electrically conducting walls exposed to an externally applied constant magnetic field B oriented perpendicular to the ducts axis. Hartmann numbers and Reynolds numbers are investigated in the following range: $M = 0 \rightarrow 5 \cdot 10^3$ $Re = 2 \cdot 10^3 \rightarrow 1.2 \cdot 10^5$. The investigation includes both the isothermal flow and the non isothermal case. In the non-isothermal configuration one wall of the duct which is aligned with the magnetic field is heated. The heat flux is perpendicular to the magnetic field and perpendicular to the main flow direction. Experimental results of the MHD flow are compared to the ordinary hydrodynamic (OHD) flows at the same hydraulic parameters. Further, the experimental MHD and OHD results are compared to numerical calculations.

First, the results for the isothermal flow are summarized.
For Hartmann numbers $M \geq 10^3$ and $N \geq 60$ the measured pressure gradient is independent of the interaction parameter. It coincides within a few percents with the values calculated for two-dimensional MHD flows. At lower M and N the inertia-less limit, governed by electromagnetic-viscous interaction is left and higher pressure gradients are obtained. For Hartmann numbers $M \leq 10^2$ and $Re \geq 10^5$ the pressure gradient corresponds to the ones known from turbulent OHD. The Reynolds number Re_{crit} where the pressure gradient is no longer affected by MHD is approximately $Re_{crit} \approx 100 \cdot M$.

Probe measurements within the fluid reveal that the velocity profile is not fully developed even for more than 16 characteristic length after entering the homogeneous magnetic field region. The side layer thickness δ_d increases along the flow direction x approximately according to the power law $\delta_d \sim x^{-1/3}$, which is characteristic for MHD flows governed by electromagnetic-inertial interaction.

Regarding the core velocity, a perfect agreement between calculated and measured data has been found for all M and N investigated. Also the shape of the velocity profiles correspond qualitatively to the calculated ones as long as the MHD flow remains laminar. The side layer velocities measured, however, are smaller than predicted and the side layers are thicker even for the laminar MHD flow.
If the Reynolds number is increased to values $Re \geq 8 \cdot 10^3$ at a Hartmann number $M = 4840$ the side layer gets unstable and velocity fluctuations appear. The velocity fluctuations are confined to the region of the side layers and do not penetrate into the core flow. As the Hartmann number decreases the critical Reynolds number for laminar-turbulent transition increases because the velocity gradient within the side layer responsible for the onset of fluctuations gets weaker. The turbulence intensities grow in magnitude with increasing Re at a constant M. The turbulence intensity, however, alters its shape in different Reynolds number regimes. At a constant Re and decreasing Hartmann number the turbulence intensity decreases in magnitude.

In case of the non-isothermal flow the following results are obtained:
The velocity profiles and the turbulence intensities measured in the isothermal and the non-isothermal campaigns differ only marginally for any parameter set investigated. Thus, the temperature acts as a passive scalar in the studied setup as long as $M \gg 1$. Both, the calculated and the measured temperatures in the fluid near the wall in the laminar MHD flows are lower than in laminar OHD flows at the same Reynolds number, because MHD flows form high velocity jets near walls aligned with the magnetic field. The measured temperature distributions of the laminar MHD flow within the fluid agrees quantitatively with the numerically predicted values. The temperatures measured in the MHD flow for any parameter set investigated are significantly smaller than the values predicted by the slug-flow model, which has been used in the design calculation of liquid metal fusion blankets. Increasing Hartmann numbers lead to higher side wall velocity jets and, therefore, to lower temperatures at the fluid-wall interface of the heated wall. Thus, an increasing magnetic field strength increases the heat transfer (, but also requires higher pumping power!). At the same Reynolds numbers laminar MHD flows show higher Nusselt numbers than their laminar OHD counterparts.

If the MHD flow gets turbulent three different heat transfer regimes appear at a Hartmann number of $M = 4993$.

- For only weak turbulence levels, where the turbulence intensity in the side wall region is less than 0.1 ($Re \leq 1.8 \cdot 10^4$), the temperature distribution corresponds to the ones for conductive heat transport. Nevertheless, the temperatures measured and calculated are in any case lower than those measured and predicted for a turbulent OHD flow. Thus, the heat transfer rates in laminar MHD flows are higher than in OHD.

- If the Reynolds number is further increased an intense heat transfer from the hot wall towards the core flow is measured and the heat transfer enhancement found in the measurements is a factor two higher than calculated with the laminar models.

- A further increase of the Reynolds number, however, does not lead to an increased heat transfer because the thermal boundary layer has not penetrated into the region of highly turbulent flow and thus the heat transfer is still governed by conduction.

The splitting into three regions of heat transfer is characteristic for thermally developing flows. The experimental results revealed that a drastic heat transfer enhancement compared to a laminar MHD flow is only obtained in a small bandwidth of Reynolds numbers. Nevertheless, the heat transfer rates of both laminar and turbulent MHD flows are in all cases higher than that of OHD flows at the same Re. They are drastically larger than the values calculated using the slug flow model, which formed the basis for many previous blanket design calculations. Properly chosen flow conditions can increase the heat transfer by a factor of 2.

Chapter 7

References

BARLEON, L., LENHART, L., MACK,K.-J., STERL, A., THOMAUSKE, K. 1989 Investigations on liquid metal MHD in straight ducts at high Hartmann numbers and interaction parameters. *Proc. of 4th Int. Top. Meet. on Nuclear Reactor Thermal-Hydraulics NURETH-4, 10th – 13th* Oct. 1989; *Karlsruhe,* **2**, 857-862.

BARLEON, L., CASAL, V., LENHART, L. 1991 MHD-flow in liquid metal cooled blankets. *Fusion Engineering and Design*, **14**, 401-412.

BARLEON, L.; MACK, K.-J.; STIEGLITZ, R. 1996 The MEKKA-facility a flexible tool to investigate MHD-flow phenomena. *FZKA-5821*, September 1996.

BLUMS, E., MIKHAILOV, Y., OZOLS, R. 1987 Heat and mass transfer. *World Scientific Publishing Co. Pte Ltd, ISBN 9971-50-112-0.*

BRANOVER, H.; VASIL'EV, A.S. 1978a Flows in mercury pipes with insulated and conducting walls under a transverse magnetic field. *Magnitnaya Gidrodinamika* **4**, 80-85.

BRANOVER, H. 1978b Magnetohydrodynamic flow in ducts. *Halsted Press; ISBN 0-470-26539-6.*

BRANOVER, H. 1986 Turbulence and the feasibility of self-cooled liquid metal blankets for fusion reactors. *Fusion Technology*, **10**, 822-829.

BÜHLER, L. 1993 Convective-diffusive transport in laminar MHD-flows. *KfK-5241.*

BURR, U. 1997 Turbulente Transportvorgänge in magnetohydrodynamischen Kanalströmungen. PhD Thesis University Karlsruhe.

CUEVAS, S., RAMOS, E., PICOLOGLOU, B.F. 1996 Turbulent liquid metal flow in rectangular ducts with thin conducting walls and strong magnetic fields. *Proc. 8th Beer-Sheva Int. Sem. on MHD flows and Turb.*, Febuary 1996, Jerusalem, p.1-13.

CUEVAS, S., PICOLOGLOU, B.F., WALKER, J.S., TALMAGE, G. 1997 Liquid metal MHD flow in rectangular ducts with thin conducting or insulating walls: Laminar and turbulent solutions. *Int. J. Engng. Sci.* **35** (5), 485-504.

CUEVAS, S., PICOLOGLOU, B.F., WALKER, J.S., TALMAGE, G. 1997b Heat transfer in laminar and turbulent liquid metal MHD flows in square ducts with thin conducting or insulating walls. *Int. J. Engng. Sci.* **35** (5), 505-514.

DAVIDSON, P.A. 1995 Magnetic damping of jets and vortices. *J. Fluid Mech.* **299**, 153-186.

FIDAP 1993 Theory Manual -Fluid dynamics analysis package. *Fluid Dynamics International Inc.,* 500 Davis Street, Suite 600, Evanston, Illinois 60201.

GARDNER, R.A. 1967 Laminar pipe flow in a transverse magnetic field with heat transfer. *Int. J. Heat Mass Transfer* **11**, 1076-1081.

GIANCARLI, L. 1994 Water-cooled Pb-17Li DEMO blanket line . EU reference conceptual desing and performance presentation. *Report DMT 94/538 (SERMA/LCA/1678).*

GRINBERG, G.K.; KAUDZE, M.Z.; LIELAUSIS, O.E. 1985 Local MHD-resistances on a liquid sodium circuit with a superconducting magnet. *Magnetohydrodynamics* **21**(1), 99-103.

HARTMANN, J. 1937 The theory of the laminar flow of an electrically conductive liquid in a homogeneous magnetic field; *Det. Kgl. Danske Videnskabernes Selskab, Mathematisk-fysiske Meddelelser,* Vol. **XV**, 1-45.

HOLROYD, R.J.; WALKER, J.S. 1978 A theoretical study of the effects of wall conductivity, non-uniform magnetic fields and variable area ducts on liquid metal flows at high Hartmann number. *J. Fluid Mech.* **84** Part 3, 471-495.

HOLROYD, R.J. & MITCHELL, J.T.D. 1984 Liquid Lithium as a coolant for Tokamak Reactors. *Nuclear Engineering and Design/Fusion* **1**, 17-38.

HUA, T. Q., GOHAR, Y. 1995 MHD pressure drop and thermohydraulic analysis for the ITER breeding blanket design. *Fusion Engng. Design* **27**, pp. 696.

HUNT, J.C.R. 1965 Magnetohydrodynamic duct flow in rectangular ducts. *J. Fluid Mech.* **21**(4), 577-590.

HUNT, J.C.R.; LEIBOVICH,S. 1967 Magnetohydrodynamic duct flow in channels of variable cross-section with strong transverse magnetic fields. *J. Fluid Mech.***28**,. 241-260.

HUNT, J.C.R.; BRANOVER, G.G.; GEL'FGAT, YU. M. 1969 Magnetohydrodynamic flow in a rectangular channel with walls of finite conductivity. *Magnitnaya Gidrodynamika* **5**(3), 139-142.

JISCHA, M. 1982 Konvektiver Impuls-, Wärme- und Stoffaustausch. Vieweg Verlag; *ISBN 3-528-08144-9*; p.188 ff.

JOHN, H., MALANG, S., SEBENING, H. (eds.) 1991 DEMO relevant test blankets for NET/ITER. *KfK-4908.*

KIRILLOV, I., REED, C.B., BARLEON, L., MIYAZAKI, K. 1995 Present understanding of MHD and heat transfer phenomena for liquid metal blankets. *Fusion Eng. Design,* **27**, 553-573.

KOLESNIKOV,Y. , TSINOBER, A. 1972 Two-dimensional flow behind a circular cylinder. *Magnetohydrodynamics* **8**, 300-307.

KOLLIE, T.G.; ANDERSON, R.L.; HORTON, J.L.; ROBERTS, M.J. 1977 Large thermocouple thermometry errors caused by magnetic fields. *Rev. Science Instrum.* **48** (5), 501-511.

LIELAUSIS, O.A. 1975 Liquid-metal magnetohydrodynamics. *Atomic Energy Review* **13**, 527-581.

MALANG, S., BARLEON, L., BÜHLER, L., DECKERS, H., MOLOKOV, S., MÜLLER, U., NORAJITRA, P., REIMANN, J., REISER, H., STIEGLITZ, R. 1993. MHD work on self-cooled liquid metal blankets under the development at the nuclear research center Karlsruhe. *Persepectives in Energy* **2**, 303-312.

MOLOKOV, S. 1993 Fully developed liquid-metal flow in multiple rectangular ducts in a strong uniform magnetic field. *Eur. J. Mech./B Fluids* **12** (6), 769-787.

MOLOKOV, S. & BÜHLER, L. 1994 Liquid metal flow in a U-bend in a strong uniform magnetic field. *J. Fluid Mech.* **267**, 325-352.

MOLOKOV, S., BÜHLER, L., STIEGLITZ, R. 1994 Asymptotic structure of MHD-flows in bends. *Proc. of the 2^{nd} Int. Conf. on Energy Transfer in MagnetoHydro-Dynamic Flows*, **2**, 473-484.

MOREAU, R. Magnetohydrodynamics. *Kluwer Academic Publishers. ISBN 0-7923-0937-5.*

O'DONELL, J.O.; PAPANIKOLAOU, P.G. & REED. C.B. 1989 The thermophysical transport properties of eutectic NaK near room temperature. *ANL/FPP/TM-237.*

REED, C.B., LYKOUDIS, P.S. 1978 The effect of a transverse magnetic field on shear turbulence. *J. Fluid Mech.* **89**, 147-171.

REED, C.B.; PICOLOGLOU, B. F. 1989 Sidewall instabilities in liquid metal MHD-flow under blanket relevant conditions. *Fusion technology* **15**; 705-715.

RHODI, W. 1985 Turbulenzmodelle und ihre Anwendung . Scriptum zur Vorlesung an der TH Karlsruhe 1985/86.

SOMMERIA, J. , MOREAU, R. 1982 Why, how and when MHD turbulence becomes two-dimensional. *J. Fluid Mech.* **118**, 507-518.

ROSSANT, M. 1976 Ecoulements hydromagnetiques turbulents en conduites rectangulaires. *These, Grenoble.*

STIEGLITZ, R., BARLEON, L., BÜHLER, L., MOLOKOV, S. 1995 Magnetohydrodynamic flow in a right angle bend in a strong magnetic field. *J. Fluid Mech.*, **326**, 91-123.

STIEGLITZ, R., MOLOKOV, S. 1997 Experimental study of magnetohydrodynamic flows in electrically coupled bends. *J. Fluid Mech.*, **343**, 1-28.

TILLACK, M.S. 1990 Magnetohydrodynamic flow in rectangular ducts. Design equations for pressure drop and flow quantity. *UCLA-FNT-41.*

TSINOBER, A. 1975 Magnetohydrodynamic turbulence. *Magnetohydrodynamics* **11**, 5-17.

WALKER, J.S. 1981 Magnetohydrodynamic duct flows in rectangular ducts with thin conducting walls, Part I. *Journal de Mècanique* **20** (1), 79-112.

ZIEREP, J. 1982 Grundzüge der Strömunglehre. G. Braun Verlag Karlsruhe. *ISBN 3-7650-2033-8*, p.122ff.

ZIEREP, J., BÜHLER, K. 1991 Strömungsmechanik. Springer-Verlag. *ISBN 3-540-53827-5*, p.88.

Appendix A

The k-ε Model

The $k-\varepsilon$ model has been used to calculate the turbulent OHD flow and heat transfer in the investigated geometry. Here, a brief overview with the constants used is gieven. Due to the non-linearity of the governing equations for a time-dependent flow a temporal averaging process introduces correlations between the fluctuating velocities $\overline{uv}, \overline{uw}, \overline{vw}$ in the momentum equation (2.1) and the temperature fluctuations $\overline{uT}, \overline{vT}$ in the energy equation (2.2). Physically, these correlations represent the transport of momentum and heat due to the fluctuating motion. The velocity correlations act like a stress on the fluid and is, therefore, called the Reynolds stress tensor. It characterizes the effect of turbulent eddy behavior on the mean flow. Similarly the temperature-velocity-correlation is a turbulent heat flux. In most flow regions the turbulent stresses and fluxes are much larger than their laminar counterparts. The extended equations for the mean values of velocity, pressure and temperature can only be solved when the turbulence correlations can be determined in some way. A turbulence model must be introduced which approximates the correlations in some manner, typically by expressing them in terms of mean-flow quantities. The most widely used approach to modeling the Reynolds stresses is the eddy viscosity concept, which assumes that the components of the Reynolds stresses are proportional to the mean velocity gradients, i.e.

$$\overline{u_i u_j} = \frac{\mu_t}{\rho} \left(\partial_{i,,j} u + \partial_{j,i} u \right). \tag{A.1}$$

The proportionality factor μ_t is termed the eddy viscosity and is unlike the molecular quantity of the viscosity μ. In a similar way a turbulent thermal conductivity λ_t can be introduced in a way that

$$\lambda_t = \frac{c_p \mu_t}{Pr_t}, \tag{A.2}$$

where Pr_t is the turbulent Prandtl number. In the classical *$k-\varepsilon-$turbulence model* the turbulence field is characterized in terms of two variables, the turbulent kinetic energy k which is defined by

$$k = \frac{1}{2}\overline{u_i u_i}, \tag{A.3}$$

and the viscous dissipation rate of the turbulent kinetic energy ε given by

$$\varepsilon = \nu \overline{u_{i,j} u_{i,j}} = \nu \int_t^{t+\Delta t} \hat{u}_{i,j} \hat{u}_{i,j}\, dt. \tag{A.4}$$

Typical turbulent eddy velocity and length scales (denoted by u_t and l_t) may be characterized as $\sqrt{k}$ and $k^{1.5}/\varepsilon$. An extension of this dimensional reasoning also leads to an expression for μ_t in terms of the characteristic scales of the turbulent eddies

$$\mu_t \sim \frac{k^2}{\varepsilon}. \tag{A.5}$$

Thus, the turbulent eddy viscosity μ_t is directly related to k and ε. A transport equation for k can be obtained from the Navier-Stokes equations by a sequence of algebraic manipulations. This transport equation contains a number of unknown correlations. A second transport equation for ε can also be derived from the Navier-Stokes equations. Application of a number of modelling assumptions simplifies these two equations to the well known equations of turbulent kinetic energy and viscous dissipation of the *$k-\varepsilon-$turbulence model*, see e.g. Jischa (1982). If all algebraic relations are introduced the eddy viscosity is given by

$$\mu_t = \rho \cdot c_m \frac{k^2}{\varepsilon}, \tag{A.6}$$

and seven empirical constants $Pr_t, \sigma_k, \sigma_E, c_m, c_1, c_2$ and c_3. Since the aim of the present experiment is not to determine the constants of the turbulence constants the standard set of constants given by Rhodi (1985) has been used in the calculations, which reads to

$$Pr_t = 0.9; \sigma_k = 1; \sigma_E = 1.3; c_m = 0.09; c_1 = 1.44; c_2 = 1.92; c_3 = 0.8. \tag{A.7}$$

The choice of this constants may be problematic in the turbulent flow regime for $Re \leqq 10^4$ because buoyant effects can not be neglected in the experiment in that regime. However, the physical effects leading to disagreements between experimental and theoretical results will be highlighted in the discussion.

Finally, the inlet distribution of k and ε must be set in the calculation as an initial condition. As initial values for k and ε at the entrance of the duct ($x = -16.7$) the values $k = 5 \cdot 10^{-3}$ and $\varepsilon = 5 \cdot 10^{-3}$ where set at each grid point of the whole duct cross-section except for the wall region. The chosen values for k and ε assume homogeneous turbulence. These values are proposed by Rhodi (1985) as starting conditions for a homogeneous grid turbulence. The assumption of homogeneous grid turbulence is justified for the investigated test section, because at the entrance of the test section a flow straightener is installed.